Structural Durability & Health Monitoring

Tech Science Press

DOI: 10.32604/sdhm.2024.058501

ARTICLE

Effect of the Aspect Ratio of Box Girders on the Buffeting Response of Long-Span Suspension Bridges

Jingxiang Zhou[1], Qiaoling Zhou[1,*], Chunlian Liang[1], Yulu Guo[1], Zhao Xiao[2] and Yingfeng Xu[1]

[1]School of Civil Engineering, Chongqing Jiaotong University, Chongqing, 400074, China

[2]School of Civil Engineering, Chongqing University, Chongqing, 400015, China

[*]Corresponding Author: Qiaoling Zhou. Email: 622220970109@mails.cqjtu.edu.cn

Received: 13 September 2024 Accepted: 25 November 2024 Published: 30 June 2025

ABSTRACT

Streamlined box girders serve as a prevalent choice for the primary structural elements in large-span suspension bridge designs. With the increase in traffic demands, the design of such girders is evolving towards wider bridge decks and larger aspect ratios (B/D). To obtain more effective and aerodynamic design shapes for streamlined box girders, it is essential to investigate the impact of B/D on their aerodynamic performance. Accordingly, in this study we investigate the buffeting responses of large-span suspension bridges using girders of varying aspect ratios (B/D of 7.5, 9.3, and 12.7). First, the aerodynamic coefficients of these girders are estimated using computational fluid dynamics (CFD) simulations. Subsequently, spatial finite element (FE) models of three long-span suspension bridges with different girders (B/D of 7.5, 9.3, and 12.7) are established in Ansys software, and the dynamic characteristics of these bridges are obtained. Then, the time-domain buffeting analysis is performed by simulating the fluctuating wind fields acting on the bridge through the spectral representation method. Ultimately, the buffeting responses are computed using Ansys software, and the impact of B/D on these responses is assessed. The results reveal that the root mean square (RMS) values of the main girder's buffeting displacement are highest at the mid-span position and are lowest at the ends of the bridge. A decrease in B/D of the main girder leads to a more severe buffeting response because both the range and the effective value of the displacement increase with the decreasing B/D. Comparing the buffeting displacements in three directions, B/D plays a significant role in the vertical buffeting displacement, moderately impacts the torsional displacement, and has the least effect on the lateral displacement. The findings of this study may help wind resistance analysis and design optimization for bridges.

KEYWORDS

Long-span suspension bridge; buffeting response; aspect ratio; streamlined box girder; turbulent flow

List of Symbols and Abbreviations

B, D, L	Width, height and length of the main girder
CFD	Computational fluid dynamics
RMS	The root mean square
LES	Large Eddy Simulation
F_D, F_L, F_M	Drag, lift and pitching moment
U	Wind speed

λ_s	The sag of the main cable
E_{eq}	The equivalent elastic modulus after ERNST correction
$S(\omega)$	The power spectral density matrix
$H^{T*}(\omega)$	The conjugate transposed matrix of H (ω)
θ_{ml}	A random phase angle uniformly distributed over [0, 2π]
U_{s10}	The basic wind speed at the bridge site, U_{s10} = 28.1 m/s
K_c	The conversion coefficient
λ_{ij}	The attenuation factor
U_y	The lateral displacement of the main girder element
$L_b(t)$, $D_b(t)$, $M_b(t)$	The lift, drag forces and pitching moment under the turbulent wind
$S_a(\omega)$	Represents buffeting lift force, buffeting drag force and buffeting pitching moment, respectively (the subscript a takes L, D, M)
$P(t)$	The external load of the bridge
α, β	The mass damping coefficient and stiffness damping coefficient
B/D	Aspect ratio
FE	Finite element
VIV	The vortex-induced vibrations
AoA	Angle of attack
ρ	The air density, usually 1.225 kg/m^3
C_D, C_L, C_M	The coefficients corresponding to the three components of aerostatic forces (AFC)
H	The initial chordal force of main cable
E_0	The initial elastic modulus of main cable
$H(\omega)$	The lower triangular matrix
ω_{ml}	The frequency of fluctuating wind speed power spectrum, the range of j values is from 1 to n; the range of l values is from 1 to n
U_d	The design wind speed at Z height from the ground
K_f	Wind resistance risk coefficient k_f = 1.02
$Coh_{ij}(\omega)$	The spatial correlation function
U_z	The vertical displacement of the main girder element
ROTx	The torsional displacement of the main girder element
$C'_L(\alpha)$,$C'_D(\alpha)$, $C'_M(\alpha)$	The derivative of the coefficients corresponding to the three components of forces (AFC) to the angle of attack (α)
$S_b(\omega)$	Represents the power spectra of the fluctuating wind in longitudinal and vertical directions, respectively (the subscript b takes u and w)
C	The stiffness matrix
$v(t)$, $\dot{v}(t)$, $\ddot{v}(t)$	Represent displacement, velocity, and acceleration vectors, respectively

1 Introduction

Large-span bridges are vital for crossing rivers, seas, mountainous areas, and hills, which can help alleviate traffic issues. As a result, large-span bridge projects have been established along the national trunk line corridors in the coastal and southwestern regions of China. Streamlined box girders are commonly employed in suspension bridges for their excellent wind resistance. However, as the spanning capacity of a bridge increases, the structural stiffness and vibration frequency gradually decrease, making the structure more sensitive to wind [1,2]. This makes wind resistance issues of the bridge more significant, rendering its aerodynamic performance a crucial aspect of the structural design process [3]. The aerodynamic performance of a streamlined box girder is highly influenced by many factors,

including aspect ratio (B/D), turbulence intensity, turbulence integral scale, nozzle, and Reynolds number. Therefore, extensive research has been conducted on these topics [4−6].

Complex wind conditions, often encountered by bridges, represent turbulent wind fields in atmospheric boundary layers. In this situation, the wind field may induce vibration of the bridge structure. Buffeting refers to a form of random forced vibration resulting from atmospheric turbulence, and any bridge in a natural environment will inevitably experience some level of wind-induced buffeting. Excessive buffeting responses can affect the comfort and safety of pedestrians and vehicles, posing a significant threat to people and the operation of traffic. Therefore, studying the buffeting responses of large-span suspension bridges under turbulent conditions holds considerable value.

In one such study, Ma et al. [5] used an active control wind tunnel test method with multiple fan arrays and oscillated airfoils to generate different turbulent wind fields, investigating the impact of turbulent characteristics on the buffeting response of streamlined box girders. As another example, Li et al. [7] investigated how the turbulence integral scale influences the buffeting response of a long-span suspension bridge, highlighting the importance of accounting for this factor in assessing the buffeting response of such structures. Zhou et al. [8] generated various wind fields featuring different turbulence integral scales through passive turbulence simulations, and examined their influence on the buffeting response of long-span suspension bridges. Moreover, Mao et al. [9] used a harmonic synthesis method to simulate spatially fluctuating wind fields, and employed time-domain vibration analysis to explore how the turbulence spatial correlation affects the buffeting response of large-span streamlined steel box girder suspension bridges. Existing research indicates that the properties of turbulent wind fields significantly influence the buffeting response of bridge sections, yet understanding of how the buffeting response relates to B/D of the main girder is limited. Meanwhile, as daily traffic increases, there is a demand for long-span suspension bridges to have greater main girder widths, encouraging the development of girder shapes with larger aspect ratios.

In order to minimize the likelihood of wind-induced vibrations during the bridge's operation, optimizing its aerodynamic performance during the design phase is essential [10,11]. Previous research has shown that optimizing the sectional shape of main girders can effectively enhance the aerodynamic performance of bridges [12−15]. In recent years, Zheng et al. [16–18] introduced a strategy for aerodynamic optimization, taking into account how changes in the cross-sectional shape influence the dynamic properties of actual suspension bridges. Montoya et al. [19] described a comprehensive computational strategy for generating the flutter response surface of a bridge and analyzed how variations in cross-sectional shape affect the aeroelastic response. Later, Montoya et al. [20] proposed a comprehensive numerical approach aimed at addressing the limitations inherent in traditional iterative processes for bridge deck shape design. However, the above shape optimizations are specific to the bridges studied.

For rectangular section structures, their aerodynamic properties and wake properties are primarily influenced by the flow separation characteristics from the leading-edge. Typically, the aerodynamic behavior of these structures can generally be classified into three distinct states based on their B/D: fully separated, intermittent reattachment, and fully reattached, with B representing the width and D representing the height of the structure, respectively [14,21,22]. The B/D of a structure plays a crucial role in determining the wind flow field distribution around it as well as its aerodynamic properties.

Given the significant impact of B/D on aerodynamic performance, many studies have been conducted in this regard. For the main girder section of a bridge, Beitel et al. [23] studied how the B/D influences the aerodynamic forces and bending moment of a cylinder. Their results confirmed the occurrence of a secondary change in the aerodynamic forces and vortex shedding at higher B/D. Ma et al. [24] performed wind tunnel experiments to examine how varying the B/D of a cylinder affects aerodynamic forces and wind pressures at the middle and along the length of the cylinder, for different flow regimes. Xing et al.

[25] conducted both experimental and numerical analyses to assess how varying B/D of bluff bodies influence the performance of energy harvesters designed for vortex-induced vibration (VIV) and galloping. Additionally, Yang et al. [26] employed two-dimensional numerical simulation to investigate how altering the height of rectangular box girder bridges affects their aerodynamic coefficients, effectively modifying the B/D in the process. Their findings indicated that increasing the height of the rectangular box girder section slightly reduced both the drag and lift coefficient associated with the main girder section. Zhang et al. [27] utilized an over mesh grid division method and computational fluid dynamics (CFD) simulations to investigate vortex-induced vibrations (VIVs) in box girder sections during construction. They revealed that the onset wind speed for VIVs varied with different aspect ratios, with a higher aspect ratio being associated with a higher onset wind speed for VIVs. Yang et al. [28] conducted wind tunnel tests using closed box girders with varying B/D, rdemonstrating the impact of these variations on flutter performance. Furthermore, Xue et al. [29] adopted three streamlined box girders featuring distinct B/D to examine how these ratios affect the force coefficients and flow separation characteristics at various angles of attack (AoA).

These findings highlight that previous studies on B/D have predominantly addressed flutter and vortex-induced vibration stability in uniform flow. However, the buffeting response of main girders under turbulent conditions remains underexplored, even though it plays a crucial role in ensuring the safety of long-span suspension bridges. The aspect ratio of streamlined box girders is a vital factor influencing the buffeting response, understanding its effects can help wind load assessments in turbulent conditions. Therefore, to address this research gap, we employ the harmonic synthesis method to generate three-dimensional turbulent wind fields and conduct time-domain analysis of buffeting responses in realistic wind environments. Specifically, this study investigates how aspect ratio influences the buffeting response of large suspension bridges, which can inform design to reduce vibration amplitudes under wind loads and mitigate structural failure risks. Additionally, we investigate the aerodynamic characteristics of bridges with varying aspect ratios, providing insights for optimizing structural forms and enhancing wind resistance during bridge design and renovation.

This study analyzes the sensitivity of buffeting responses to different B/D of the main girder, using a long-span suspension bridge as a case study. This paper is structured as follows: First, Section 2 presents the time-averaged and RMS (root mean squared) values of the aerodynamic coefficients of streamlined box girders with different B/D. Subsequently in Section 3, spatial FE models of three long-span suspension bridges with different girders (B/D of 7.5, 9.3, and 12.7) are established in Ansys software, and the dynamic characteristics of these bridges are obtained. Then, in Section 4, based on the results obtained in Sections 2 and 3, time-domain buffeting analysis is conducted to understand how the aspect ratio affects the buffeting response. Lastly in Section 5, we summarize our findings and conclusions.

2 Aerodynamic Coefficients of Streamlined Box Girders with Varying Aspect Ratios

2.1 Model and Case Setup

Informed by data from ten major long-span suspension bridges with box girders in China, the aspect ratios of the box girders are set to range from 5.3 to 13.6. To examine how the B/D impacts buffeting response, a streamlined box girder model, characterized by a B/D ratio of 9.3, is selected as the prototype. The model features a 1:90 scale ratio, with dimensions measuring 0.28 m in width and 0.03 m in height. Meanwhile, models with B/D = 7.5 and B/D = 12.7 are designed by changing the width of the model based on the prototype, as shown in Fig. 1. The cross-sectional height (D) of the main girders of all models is 0.03 m, and the widths of the 12.7, 9.3, and 7.5 main girders are 380.1, 280, and 225 mm, respectively. The extension length of the main girder model L = 3B.

The numerical simulation conditions are given in Table 1, where cases B-1, B-2, and B-3 represent the main girder models with aspect ratios of 7.5, 9.3, and 12.7, respectively.

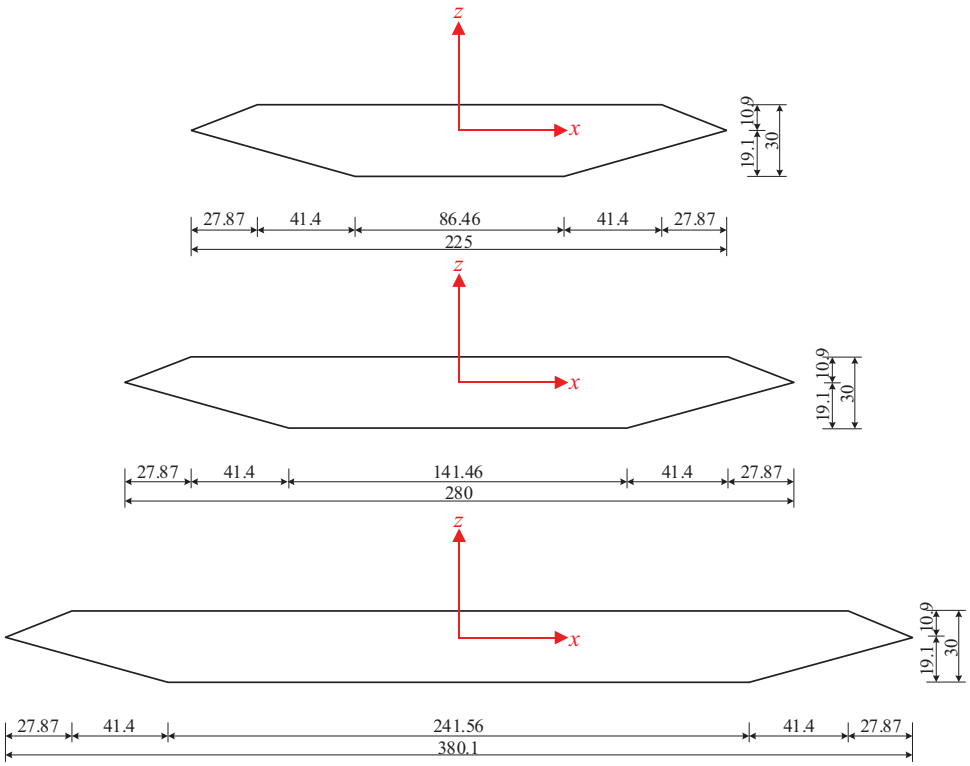

Figure 1: The section models of different aspect ratios with a scale ratio of 1:90 (unit: mm)

Table 1: Cases of box girders with varying aspect ratios

Case	Aspect ratio	Angle of attack α (°)
B-1	7.5	0°, 2°, 4°, 6°, 8°, 10°, 12°
B-2	9.3	0°, 2°, 4°, 6°, 8°, 10°, 12°
B-3	12.7	0°, 2°, 4°, 6°, 8°, 10°, 12°

2.2 Numerical Simulation Setup

2.2.1 Numerical Method

In this study, Ansys *ICEM* [30] software is used to draw the 3D computational domain mesh, and Ansys *Fluent* [30] is used for numerical simulations and post-processing of the results. The turbulence model was based on the Large Eddy Simulation (LES) model and the Smagorinsky-Lily sub-grid scale model. The pressure-velocity coupling uses the SIMPLEC algorithm, the pressure and momentum equations follow the second-order upwind scheme, and the discretization adopts the bounded second-order implicit scheme [31]. The main girder model is calculated in a steady-state uniform flow (the calculated residuals are less than 1×10^{-5}) and then adjusted to a transient model.

2.2.2 Computational Domain and Boundary Conditions

The cross-sectional shape of the main girder with a B/D of 9.3 (Model B-2) is consistent with that of the wind tunnel test model. As shown in Fig. 2, its dimensions are $19B \times 12B \times 3B$ (5.32 m × 3.36 m × 0.84 m) in the x-, y-, and z-directions, respectively. The boundary conditions of the computational domain are set as follows: the entrance is defined as a velocity-inlet boundary, the exit functions as an outflow boundary,

and the top, bottom, and side surfaces of the computational domain are symmetric boundaries. The system consists of approximately three million grid cells. The meshing distributions in the *x*–*y* plane of Model B-2 are shown in Fig. 3.

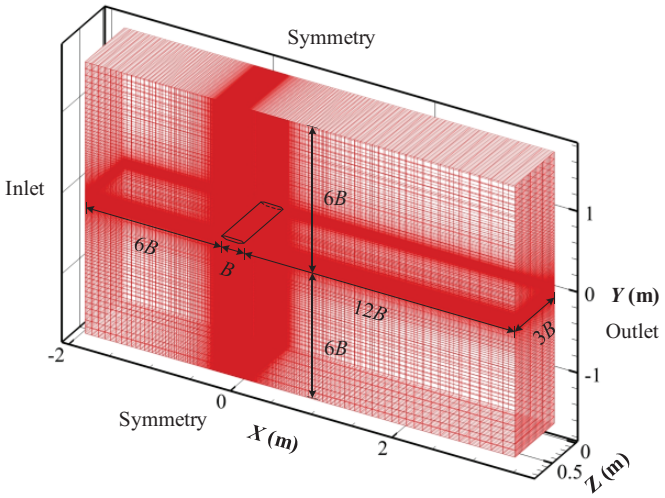

Figure 2: Computational domain and boundary conditions of Model B-1, Model B-2 and Model B-3

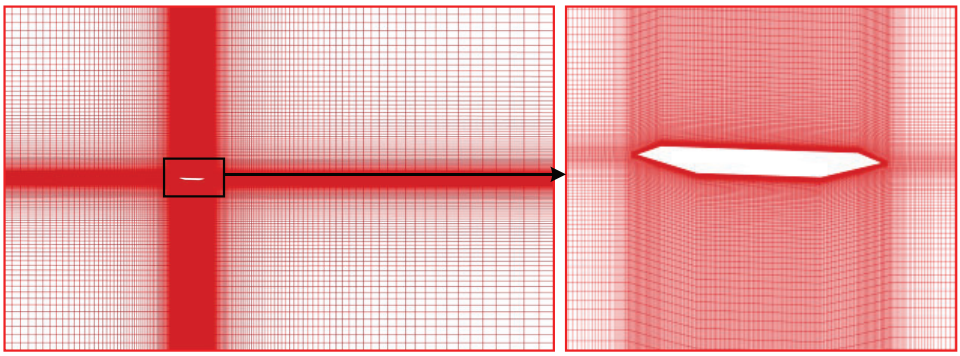

Figure 3: Meshing distributions in the *x*–*y* plane (Model B-2)

The dimensions of the computational domains of the main girder with a B/D of 12.7 (Model B-3) and the main girder with an B/D of 7.5 (Model B-1) are consistent with Model B-2, as shown in Fig. 2. The dimensions of Model B-3 are $19B \times 12B \times 3B$ (7.22 m × 4.56 m × 1.14 m) in the *x*-, *y*-, and *z*-directions, respectively, and the total number of grid cells is about 3.68 million. Meanwhile, the dimensions of Model B-1 are $19B \times 12B \times 3B$ (4.275 m × 2.7 m × 0.675 m) in the *x*-, *y*-, and *z*-directions, respectively, and the total number of grid cells is about 2.63 million. The meshing distributions of Model B-3 and Model B-1 in the *x*–*y* plane are illustrated in Fig. 4. The blockage ratio of all models is less than 3%, ensuring the independence of the computing domain [32]. For temporal discretization, the timestep is $\Delta t = 0.0005$ s, which ensures that the maximum Courant-Friedrichs-Lewy (CFL) number ($\Delta tU/\Delta x$) remains below 1.

Additionally, this paper takes Model B-2 as an example to discuss grid-independent and time-independent checking. The spatial computational domain is discretized using structured mesh, with mesh distributions determined by dependence tests to guarantee solutions that are independent of the mesh. The

corresponding results are presented in Table 2. For a better comparison of the three main girders, it should be pointed out that both lift and moment coefficient are characterized by the height of the model (D). According to the results, it can be considered that the simulation results of CFD are independent of the computational domain mesh as well as the time step.

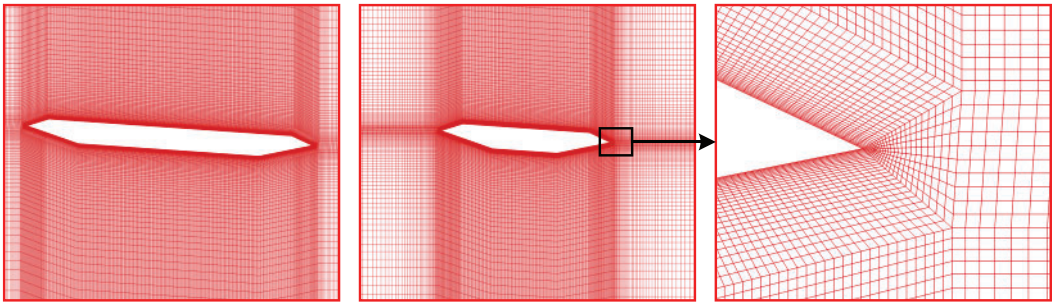

Figure 4: Meshing distributions of Model B-3 and Model B-1 in the *x–y* plane

Table 2: Results of the domain and mesh dependence studies at AoA = 0° (taking Model B-2 for example)

Grid number	Time step	Results		
		$\bar{C}_D$	$\bar{C}_L$	$\bar{C}_M$
≈68,000 × 30	0.0005	0.181	−1.718	2.665
≈10,200 × 30 (Present study)	0.001	0.189	−1.764	2.702
	0.0005 (Present study)	0.203	−1.898	2.793
	0.0002	0.207	−1.924	2.819
≈14,3000 × 30	0.0005	0.211	−1.915	2.823

2.2.3 Verification of the Computational Fluid Dynamics Results

We validate the accuracy of the numerical simulation results based on the wind tunnel tests of Li et al. [6]. As illustrated in Fig. 5, the simulated mean aerodynamic coefficients in uniform flow are compared with the experimental data, datademonstrating that the numerical results fit the experimental data well. Therefore, the chosen parameters for the numerical simulation are suitable for the current LES research method, and the numerical simulation results meet the accuracy requirements.

2.3 Aerodynamic Coefficients

Static forces result from the averaged wind speed acting on the bridge at an equilibrium state. Fig. 6 illustrates the lift (F_L), drag forces (F_D), and pitching moment (F_M) acting on the girder per unit span length, which are determined using the following equations. For a better comparison of the three main girders, it should be noted that both the lift and moment coefficient are characterized by the height of the model (D).

$$F_D = \frac{1}{2}\rho U^2 C_D(\alpha) DL \tag{1}$$

$$F_L = \frac{1}{2}\rho U^2 C_L(\alpha) DL \tag{2}$$

$$F_M = \frac{1}{2}\rho U^2 C_M(\alpha) D^2 L \tag{3}$$

In Eqs. (1)–(3), the coefficients C_D, C_L, and C_M represent the three components of the aerostatic forces (AFC); ρ is the air density, typically 1.225 kg/m^3; U is the mean wind speed; D and L denote the height and length of the model, respectively.

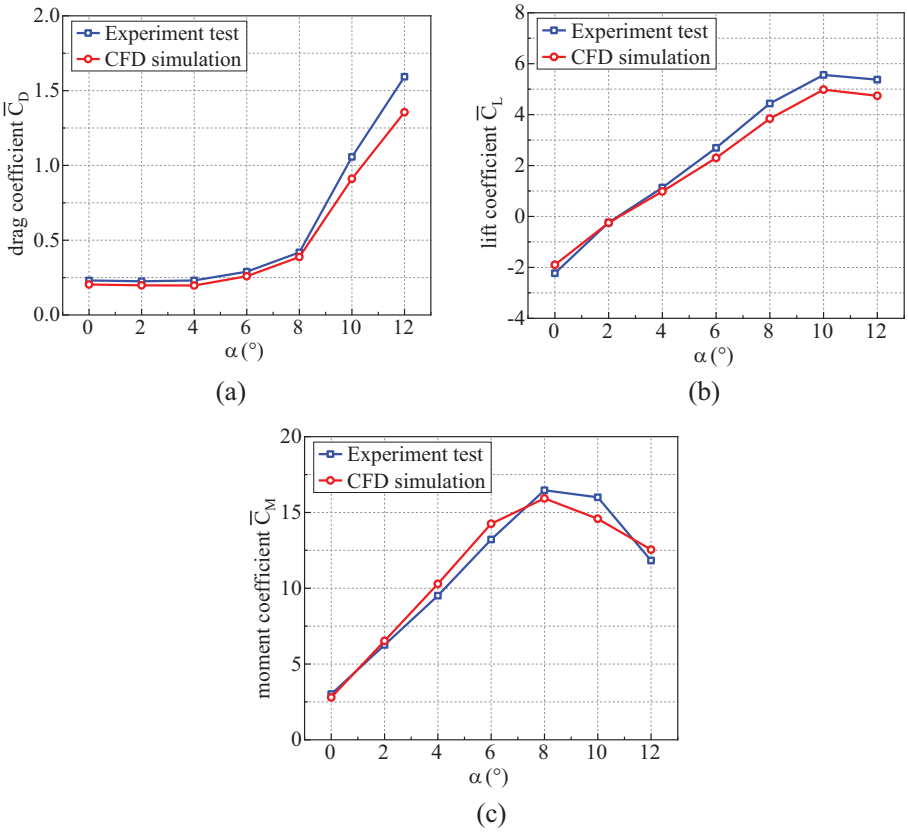

Figure 5: Comparison of aerodynamic coefficients of the box girder from simulated and test values (Model B-2) (a) Drag coefficient; (b) Lift coefficient; (c) Moment coefficient

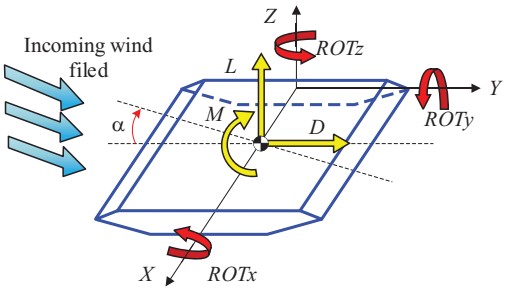

Figure 6: Diagram of the aerodynamic forces on the box girder

To study the influence of different aspect ratios on the aerodynamic coefficients of the main girder, Fig. 7 presents the variation of the mean aerodynamic coefficients with AoA for B/D of 7.5, 9.3, and 12.7.

Additionally, Fig. 8 presents the variation of the fluctuating three-component force coefficient with angle of attack for three main girders with different B/D. One of the main findings is that an increase in B/D is associated with a corresponding rise in the value of $\bar{C}_L$. Moreover, the difference in $\bar{C}_L$ is less for smaller AoA ($0° \leq \alpha \leq 4°$) and larger as the AoA increase; this trend can be attributed to the lift is mainly produced by the the differential pressure across the upper and lower surfaces. For the cases of small AoA, the streamlined box girder has a better streamlined shape, and the upper and lower surfaces of the main girder do not show the flow separation phenomenon. With the increase of the AoA, the separation bubble on the upper surface of the main girder with larger width becomes larger, which results in a larger pressure difference between the upper and lower surfaces. Accordingly, the $\bar{C}_L$ exhibits a progressive increase with the increase of aspect ratio, a change which becomes more significant at high AoA. The same phenomenon occurs in C'_L.

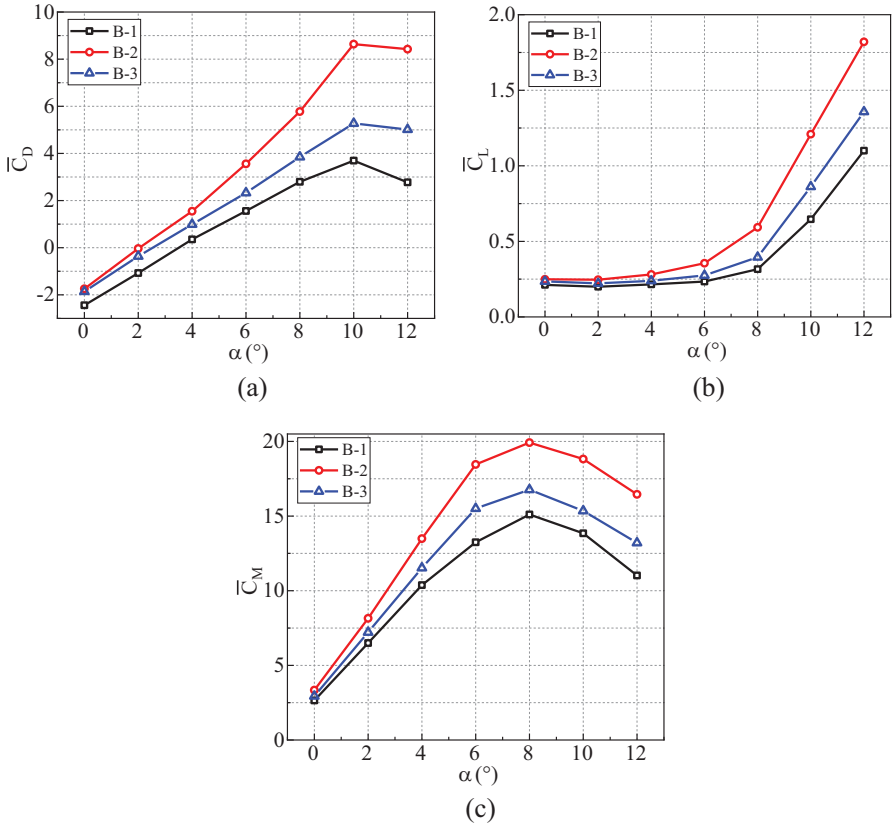

Figure 7: Effect of aspect ratio (B/D) on the time-averaged aerodynamic coefficients (a) Drag coefficient; (b) Lift coefficient; (c) Moment coefficient

The $\bar{C}_D$ value will also increase gradually with the increase in B/D. Since $\bar{C}_D$ has a strong relationship with the windward area of the main girder, for the case of small AoA, the height of the main girder is the same, and the windward area is the same. At this time, the difference in $\bar{C}_D$ is small, and the influence of B/D on $\bar{C}_D$ is also small. Meanwhile, the $\bar{C}_D$ of a small main girder stays constant at small angle of attack, and increases significantly when $\alpha \geq 6°$. When the AoA reaches 6°, the windward area of the structure with a large aspect ratio increases rapidly, and the corresponding $\bar{C}_D$ increases linearly due to the increasing B/D; this enhancement amplifies the blocking effect exerted by the main girder. At the same time, the C'_D. of the main girder increases with increasing B/D.

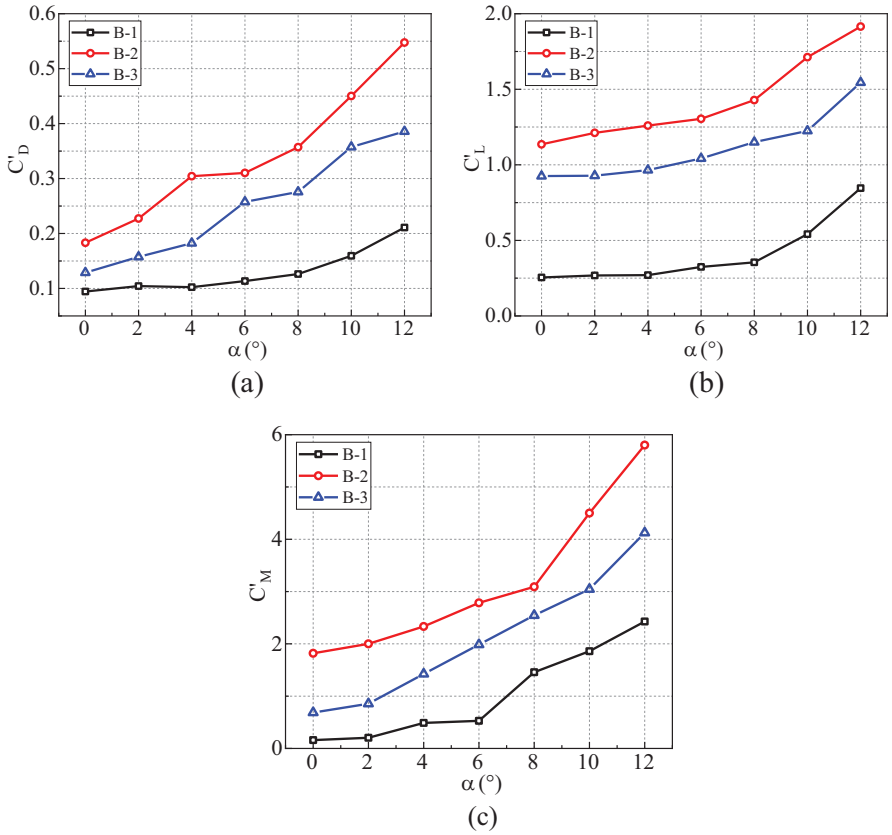

Figure 8: Effect of B/D on the RMS value of the aerodynamic coefficients (a) Drag coefficient; (b) Lift coefficient; (c) Moment coefficient

The variation of $\bar{C}_M$ for main girders with different aspect ratios is similar to that of $\bar{C}_M$ and $\bar{C}_M$. As the width of the main girder increases, the upper surface of the windward side experiences a greater flow separation phenomenon, resulting in a larger difference between the surface pressures on the windward side and the leeward side. Therefore, as B/D increases, the $\bar{C}_M$ also increases. Correspondingly, the C'_M. exhibits a progressive increase with the increasing B/D.

From the preceding analysis, we can conclude that streamlined box girders with a larger B/D ratio experience greater average and fluctuating aerodynamic force coefficients, especially in conditions with larger angles of attack. Therefore, the aspect ratio is a significant factor affecting the aerodynamic force coefficients of streamlined box girders.

3 Spatial Finite Element Models of Bridges with Girders of Different Aspect Ratios

3.1 Description of the Bridge

Based on the design scheme of a suspension bridge, a FE model of a bridge is established. Fig. 9 illustrates that the bridge comprises a main span of 880 m and two approach spans of 250 m each. The height of the towers is 100 m, and the sag-to-span ratio of the main cable is 1/8.8. The galvanized high-strength steel wire strands are employed as main cables, with one on each side of the bridge, parallel to each other, and a total of 114 boom rods in the whole bridge. Under each separate pier, there are 21 drilled and cast-in-place piles, each with a diameter of 2 m. Gravity-type anchors are used to secure both ends of the suspension bridge. The streamlined steel box girder is used for the bridge deck, with the B/D of the main girder varying at 7.5, 9.3, and 12.7 according to Fig. 1. The height of the box girder is

2.7 m, and the widths are 20.25, 25.11, and 34.2 m, respectively. The cross-section of the main girder is referred to from Fig. 1 in Section 2.1, and its scale ratio is 1:90.

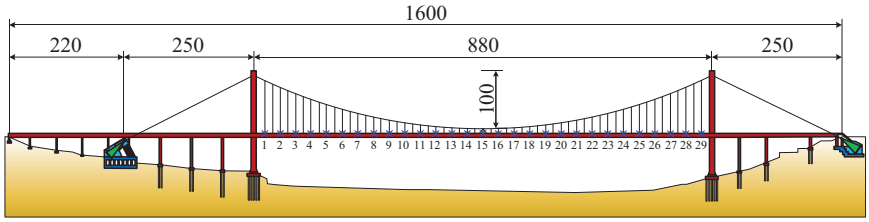

Figure 9: Layout of the bridge and wind field simulation points (unit: m)

3.2 Finite Element Modeling

Referring to modeling methods for buffeting analysis in long-span bridges [33−37], a FE model is established to capture the dynamic characteristics of the bridge and provide a basis for buffeting response analysis. The FE modeling method this research applies aligns with those utilized in the abovementioned studies. We use the APDL (Ansys Parametric Design Language) of Ansys to model the suspension bridge. In light of the mechanical characteristics of the suspension bridge structure and the design description, the constraints at the end of the suspension bridge model are simplified. Moreover, the boundary conditions of the bridge satisfy the following:

(i) The bridge towers are consolidated with caps, limiting their degrees of freedom in all directions.

(ii) The main cable and end anchorage are considered consolidated, limiting their degrees of freedom in all orientations.

(iii) The main girder and the lower beam of the tower are coupled and connected, considering the coupling degrees of freedom in the transverse, vertical, and torsional directions. The two are connected by elastic supports, limiting the longitudinal displacement.

Taking the model with an aspect ratio of 12.7 as an example, the FE calculation model of the suspension bridge is established as shown in Fig. 10. The entire 3D FE bridge model is is oriented such that the x-axis aligns with the span direction, the y-axis with the transverse direction, and the z-axis with the vertical alignment of the bridge tower. The FE modeling of the suspension bridge employs a fish-bone-girder model, which simplifies the main girder into a rectangular beam using approximate properties, such as stiffness and moment of inertia, instead of adopting a plate and shell model for the bridge deck. The bridge tower, cross beam, main girder, main cable suspender, central buckle, rigid arm, secondary dead load, and elastic support are composed of 296, 80, 58, 270, 4, 118, 59, and 2 units, respectively. The entire bridge is composed of 719 nodes and 887 units. The 8 end points of the tower bottom and anchor point are fixed ends, and the lower beam is connected with the end of the main girder by elastic supports. There are 10 constraint conditions in total. Since we focus on the dynamic characteristics of the whole bridge, the mesh of the solid model is not yet completed. For the application of external loads, the secondary dead loads are represented at the main girder nodes as mass points, by means of equivalent nodes.

The suspension bridge employs LINK10 elements for modeling both the main cables and the suspenders, and the main cables and hangers are designed as two-force members that only withstand tension and not compression (using the KEYOPT command), thus reflecting the true conditions of the bridge structure. Since the cross-section in the main span of the suspension bridge does not change, and the B/D of the cross-section is the primary variable parameter, the simpler BEAM4 elements are used to define the main girder elements. The main tower, and the upper, middle, and lower cross beams adopt BEAM44 elements to be a structure with variable cross-sections. The mass load of the bridge (secondary

dead load, mass moment of inertia, etc.) is simulated using MASS21 elements, and COMBIN14 elements are used to simulate the elastic support under the bridge cross beams.

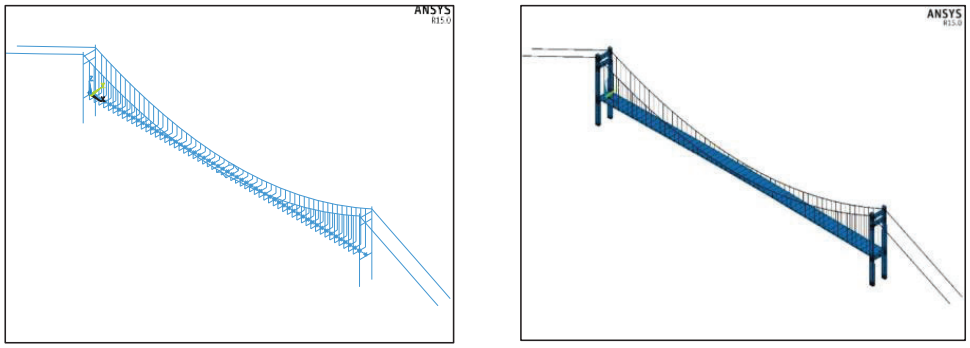

Figure 10: The FE model of the suspension bridge (Model B-3)

For the main girder formed by BEAM4 elements, the main girder element is regarded as a beam element that can be subjected to bending, compression, tension, and torsion. Under the action of drag, lift, and pitching moment, it can generate six degrees of freedom in space, as shown in Fig. 6. This section focuses on the vertical displacement U_z, lateral displacement U_y, and torsional displacement ROT_x of the main girder element, while displacements in other directions are neglected. The moment of inertia and cross-sectional area for models with varying width-to-height ratios are computed according to the specifications of the main girder's designed cross-section. Also, the real constants and parameters of the BEAM4 model are adjusted to establish the corresponding target model. The local models of the three types of bridges are presented in Fig. 11.

Because the mass, length, inclination, and diameter of the main cable have great impact on the buffeting response of the bridge, it is more complicated to analyze each separately. The comprehensive analysis of the sag of the main cable λ_s is thus performed as follows [38]:

$$\lambda_S{}^2 = \frac{(mgcos\alpha)^2}{H^3 l'} E_{eq} A_S l^3, \; l' = l\left(\frac{1+8d^2}{l^2}\right) \tag{4}$$

where m is the mass of the main cable; α is the inclination of the main cable; H is the initial chordal force of the main cable; A_S, l, d indicate the cross-sectional area, and chord length and central sag of the main cable, respectively; and E_{eq} indicates the equivalent elastic modulus after ERNST correction:

$$E_{eq} = \frac{E_0}{1 + \frac{(\gamma l_h)^2 E_0}{12\sigma_0{}^3}} \tag{5}$$

Here, E_0 is the initial elastic modulus of the main cable regardless of sag effect; γ, l_h, and σ_0 denote the bulk density, horizontal projection length, and initial stress of the main cable, respectively. In addition to the suspension bridge main cable, other material parameters for establishing the bridge FE model are shown in Table 3. The elastic modulus, Poisson's ratio, mass density, as well as other parameters of each material are determined in accordance with the *Code for Design of Steel Structures* and *Code for Design of Concrete Structures*. Among them, the elastic modulus of the custom rigid body is taken as 1000 times the elastic modulus of steel. Additionally, Table 4 presents the specific types of elements utilized in the bridge structure. In the FE modeling, the material parameters and element type settings of Model B-1, Model B-2, and Model B-3 are consistent. The difference in three models lies in the varying widths of the main

girder, which results in different physical parameters such as the cross-sectional area of the main girder, the moment of inertia in the *y*-direction and *z*-direction, as well the torsional moment of inertia in the *x*-direction.

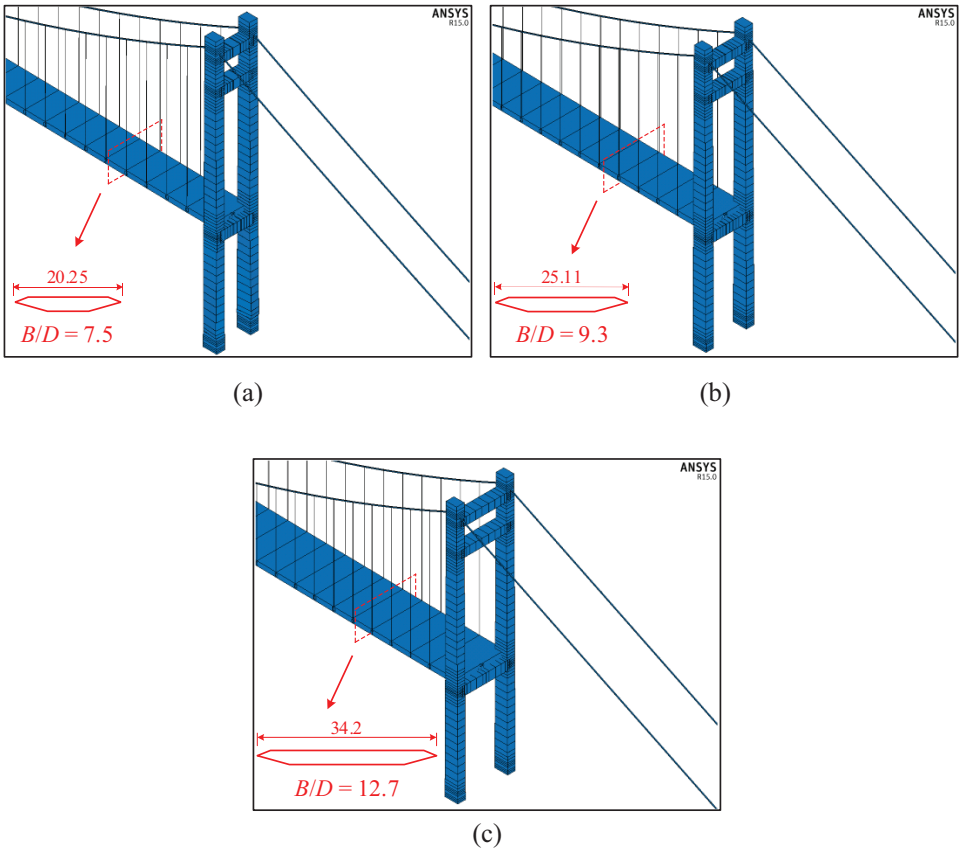

Figure 11: Detailed view of the FE models of (a) Model B-1;(b) Model B-2; (c) Model B-3 (unit: m)

Table 3: Material parameters (using Model B-3 as an example)

Number	Material type	Elastic modulus (MPa)	Poisson's ratio	Mass density (kg/m^3)	Structure type
1	High-strength steel wire	2.00×10^5	0.3	8650	Main cable, Sling
2	Q345qD	2.10×10^5	0.3	7850	Main girder
3	C50 concrete	3.45×10^4	0.2	2650	Bridge tower, Crossbeam
4	Custom rigid body	1.00×10^9	0	0	Rigid arm

3.3 Dynamic Characteristics

The first 20 natural frequencies of the bridge are calculated using the Ansys software. Usually, the high-order vibration modes of the bridge rarely occur, so Table 5 only lists the first 10 natural frequencies of the three suspension bridges. The data presented in the table indicates that with the reduction of the aspect ratio of the main girder, the width of the main girder is narrower, the stiffness of the bridge structure system is

smaller, the structural damping is smaller, and the natural vibration frequency of the bridge is lower. Therefore, the long-span suspension bridge tends to have a larger amplitude under dynamic loading.

Table 4: Element types (using Model B-3 as an example)

Model	Number	Structure type	Element type	Number of elements
Model B-3	1	Bridge tower, Crossbeam, Rigid arm	Beam44	494
	2	Main girder	Beam4	58
	3	Main cable, Sling	Link10	270
	4	Secondary dead load, Mass moment of inertia	Mass21	59
	5	Longitudinal damper	Combin14	2

Table 5: Dynamic characteristics of Model B-1, Model B-2, and Model B-3

Order	Self-vibration frequency (Hz)		
	B/D = 12.7	B/D = 9.3	B/D = 7.5
1	0.11	0.10	0.09
2	0.12	0.12	0.12
3	0.17	0.17	0.17
4	0.25	0.25	0.22
5	0.27	0.26	0.24
6	0.27	0.26	0.26
7	0.27	0.27	0.26
8	0.28	0.27	0.26
9	0.30	0.28	0.27
10	0.31	0.30	0.30

Taking the bridge model with an aspect ratio of 12.7 as an example, Fig. 12 presents the first 10 vibration modes. The stiffness and damping decrease due to the decrease of bridge width. Looking closer, the fourth-order vibration mode for aspect ratios of 7.5 and 9.3 is the first-order symmetrical yaw of the main cable, and the subsequent vibration modes are one order earlier than the bridge vibration modes of B/D = 12.7. The first three vibration modes of the three suspension bridges are the same, and the other vibration modes are similar, therefore we omit them for brevity.

Based on the dynamic characteristics obtained from the FE software, the fundamental frequency of the bridge is between 0.09 and 0.11 Hz, and the vibration modes are all first-order symmetrical transverse bending of the main girder. Additionally, the frequency of the second-order self-vibration is approximately 0.12 Hz, and the modes are all first-order symmetrical vertical bending, which conforms to the characteristics of the flexible structure of a long-span suspension bridge. Since the cross-sectional design of the streamlined box girder can provide large torsional stiffness, none of the first ten vibration modes of the bridge models exhibit torsional vibrations, making the bridge less prone to torsional deformations. Meanwhile, lateral displacement phenomena are more pronounced due to the smaller lateral bending stiffness of the bridge. As a result, the first mode corresponds to transverse bending of the main girder, while the second mode represents vertical bending. Since the stiffness of the bridge tower

significantly surpasses that of both the main girder and main cables, the first ten vibration modes are primarily characterized by the displacements of the main cables and main girders; the displacements of main tower are relatively small and can be neglected for practical purposes.

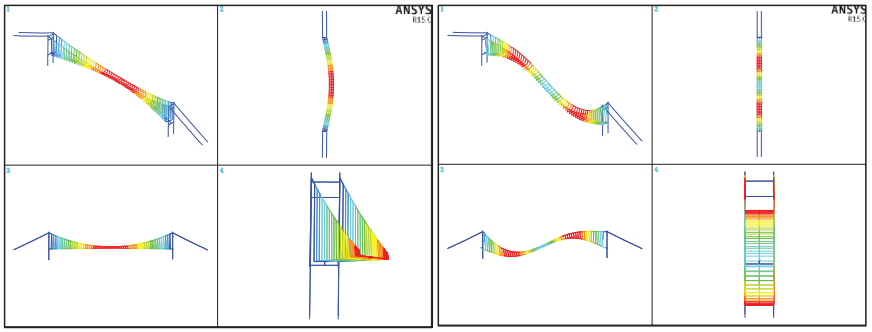

(a) Mode 1 (b) Mode 2

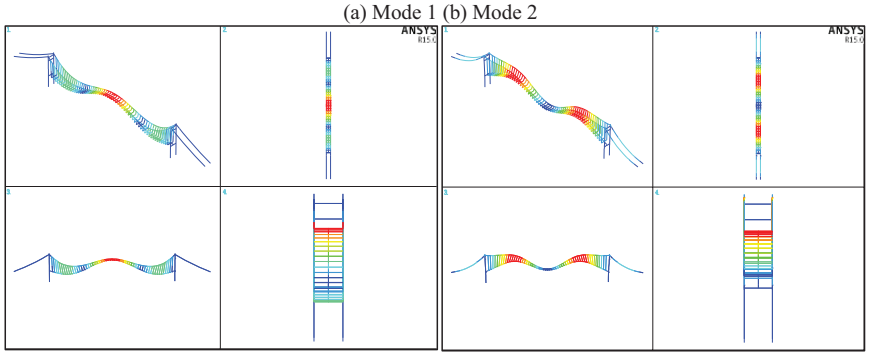

(c) Mode 3 (d) Mode 4

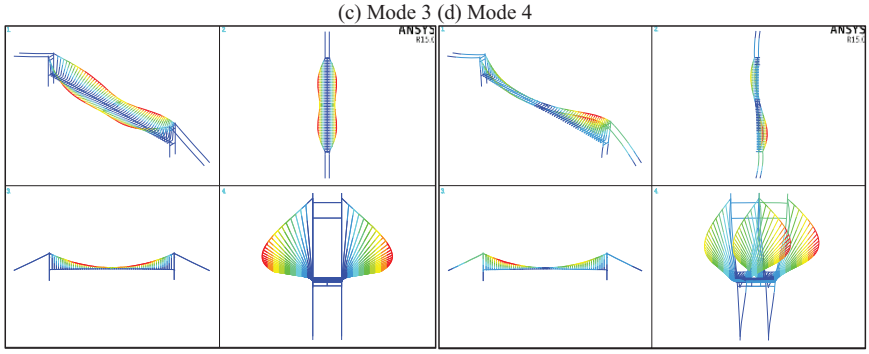

(e) Mode 5 (f) Mode 6

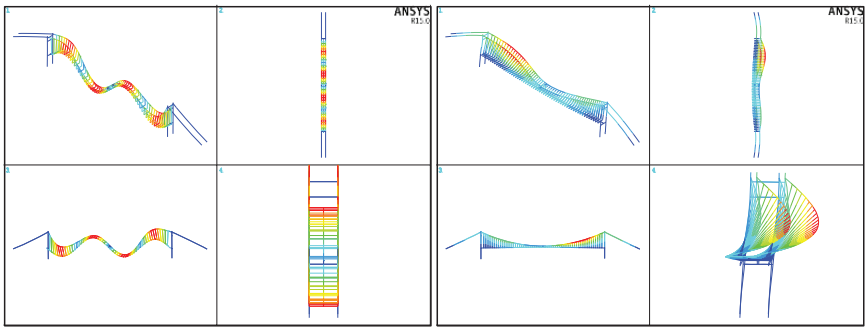

(g) Mode 7 (h) Mode 8

Figure 12: (Continued)

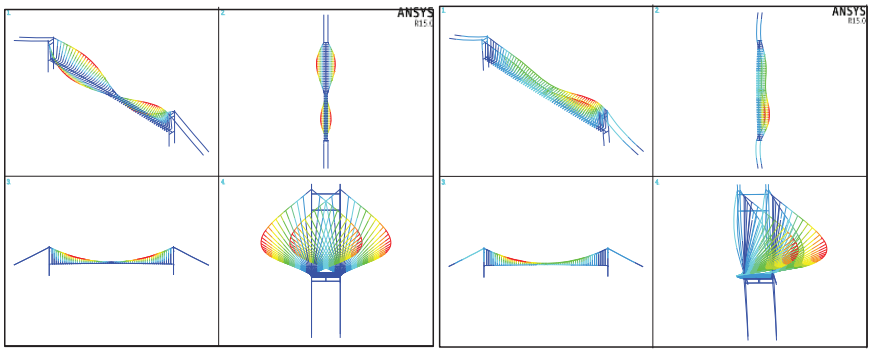

(i) Mode 9 (j) Mode 10

Figure 12: The first 10 ordered vibration modes of the suspension bridge (Model B-3)

4 Effect of Aspect Ratio on the Buffeting Responses of Long-Span Suspension Bridges

4.1 Wind Field Simulation

To assess the buffeting responses of the entire bridge in fluctuating wind conditions, the time history of the fluctuating wind speeds should be obtained first, and then imposed on various structures on the bridge in the form of dynamic excitation. Generally, the time history of fluctuating wind speed can be evaluated by field measurements and numerical simulation. The simulation of fluctuating wind fields is essentially the simulation of a random process. At present, the commonly used simulation methods for this phenomena include the linear filter method, harmonic synthesis method, and wavelet analysis method.

In 1954, the harmonic synthesis method was proposed by Rice [39] to generate turbulent wind fields satisfying Gaussian random distribution in spatial frequency domain. The basic idea of the harmonic synthesis method is derived from Fourier Series theory, can be understood as the combination of multiple of sine waves and cosine waves. The Cholesky decomposition of the power spectral density matrix $S(\omega)$ is performed first when the harmonic synthesis method is employed to synthesize a fluctuating wind field:

$$S_\omega = H_\omega \cdot H^{T*}(\omega) \tag{6}$$

$$S_\omega = \begin{pmatrix} S_{11}(\omega) & S_{12}(\omega) & \cdots & S_{1n}(\omega) \\ S_{21}(\omega) & S_{22}(\omega) & \cdots & S_{2n}(\omega) \\ \vdots & \vdots & \ddots & \vdots \\ S_{n1}(\omega) & S_{n2}(\omega) & \cdots & S_{nn}(\omega) \end{pmatrix} \tag{7}$$

where H_ω denotes a lower triangular matrix; $H^{T*}(\omega)$ represents the conjugate transposed matrix of H_ω. The diagonal elements of H_ω are usually given by a real nonnegative function expressed as:

$$H_{aa}(\omega) = \left(\frac{D_a(\omega)}{D_{a-1}(\omega)} \right)^{1/2} \tag{8}$$

And its non-diagonal elements are typically given by a complex function of ω, expressed as:

$$H_{ab}(\omega) = H_{bb}(\omega) \frac{S\begin{pmatrix} 1, & 2, & \cdots, & b-1, & a \\ 1, & 2, & \cdots, & b-1, & b \end{pmatrix}}{D_b(\omega)} \tag{9}$$

Here, $D_a(\omega)$ and $D_b(\omega)$ represent the ath and bth master-sub formulas of $S(\omega)$, where $a, b = 1, 2, \ldots, n$. By substituting Eqs. (9) and (8) into Eqs. (6) and (7), we obtain the power spectral density matrix $S(\omega)$ as:

$$S\begin{pmatrix} 1, & 2, & \cdots, & b-1, & a \\ 1, & 2, & \cdots, & b-1, & b \end{pmatrix} = \begin{pmatrix} S_{11} & S_{12} & \cdots & S_{1,b-1} & S_{1,b} \\ S_{21} & S_{22} & \cdots & S_{11} & S_{11} \\ \vdots & \vdots & \ddots & \vdots & \vdots \\ S_{b-1,1} & S_{b-1,2} & \cdots & S_{b-1,b-1} & S_{b-1,b} \\ S_{a1} & S_{a2} & \cdots & S_{a,b-1} & S_{a,b} \end{pmatrix} \tag{10}$$

When the number of terms (n) in the power spectral density matrix $S(\omega)$ approaches infinity:

$$u_j(t) = \sum_{m=1}^{j} \sum_{l=1}^{N} |H_{jm}(\omega_{ml})| \sqrt{2\Delta\omega} \cdot \cos[\omega_{ml} + \theta_{ml}] \tag{11}$$

$$\omega_{ml} = (1-1) \cdot \Delta\omega + \frac{m}{n}\Delta\omega \tag{12}$$

$$\Delta\omega = \frac{(\omega_{max} - \omega_{min})}{N} \tag{13}$$

Here, $u_f(t)$ is the fluctuating wind speed; ω_{ml} is the frequency of the fluctuating wind speed power spectrum; the range of j values is from 1 to n; the range of l values is from 1 to n; and θ_{ml} is a random phase angle that is uniformly distributed across the over [0, 2π].

The harmonic synthesis method is capable of producing turbulent wind fields satisfying the target fluctuating wind speed power spectrum and correlation function. In this paper, the turbulent wind field at the entrance is created using the harmonic synthesis method, and then the target wind field satisfying the turbulent characteristics is generated, and the buffeting response of suspension bridge is analyzed accordingly.

4.1.1 Wind Field Simulation Parameters

(1) Simulation parameter setting

According to *Wind-resistant Specification*, the wind profile parameters at the bridge site are determined by the following formulas:

$$U_d = k_f \left(\frac{Z}{10}\right) U_{s10} \tag{14}$$

$$U_{s10} = k_c U_{10} \tag{15}$$

where U_{dU} denotes the design wind speed at a height Z from the ground; U_{s10} represents the basic wind speed at the bridge site, U_{s10} = 28.1 m/s; the conversion coefficient k_c = 1.0; the wind resistance risk coefficient k_f = 1.02; and the surface roughness coefficient α_0 = 0.166. We substitute the known values into Eqs. (14) and (15) to obtain the design wind speed expression at height Z from the ground as:

$$U_d = 28.662 \times \left(\frac{Z}{10}\right)^{0.166} \tag{16}$$

The spatial correlation function of the turbulent wind field is transformed into the expression of circular frequency using Davenport's model:

$$Coh_{ij}(\omega) = exp\left(-\lambda_{ij}\frac{\omega\gamma_{ij}}{2\pi U_d}\right) \tag{17}$$

where $Coh_{ij}(\omega)$ is the spatial correlation function; λ_{ij} is the attenuation factor, taken as 7; ω is the circular frequency; and the rest of the quantities are the same as above.

The power spectrum characterizing the fluctuating wind speed in a turbulent wind field follows the power spectrum of longitudinal fluctuating wind speed as proposed by Von Kármán, which is converted into a function of time (t):

$$\frac{nS_u(n,z)}{{u_*}^2} = \frac{4t}{(1+70.78t^2)^{5/6}},\ t = \frac{nL_u^x}{U(z)} \tag{18}$$

Here, the quantities are the same as above.

(2) Layout of the wind field simulation points

Practically, the height of the main girder above the ground is Z = 122.8 m, for which the design wind speed is calculated as 43.46 m/s by Eq. (16). The arrangement of the fluctuating wind speed points is along the span direction of the main girder. Simulation points are set at intervals of 30 m in the x-direction along the main girder, numbered from 1 to 29 (a total of 29 points). The layout of the fluctuating wind speed simulation points is presented in Fig. 9. To summarize, Table 6 lists the main parameter settings for the generation of turbulent wind fields using harmonic synthesis.

Table 6: Main parameter settings for the wind field simulation

Parameter name	Value	Parameter name	Value	Flow field characteristics
Design reference wind speed at the main girder (m/s)	43.46	Cut-off frequency ω_u (rad/s)	3π	(I_u = 7.34%, L_u = 0.525 m)
Surface roughness coefficient α_0	0.166	Temporal distance of wind speed (s)	0.25	
Number of simulation points on the bridge deck	29	Number of frequency samples	1024	
Simulate point distance (m)	30	Duration of the simulation T (s)	600	
Attenuation factor λ_{ij}	7	Target power spectral density function	Von Kármán spectrum	

4.1.2 Results of the Wind Field Simulation

Using the harmonic synthesis method, fluctuating wind speeds at 29 simulation points on the main girder are generated. The time series of longitudinal wind speeds for three typical points are shown in Fig. 13. From the figure, we observe that the simulated longitudinal turbulent wind speed along the main girder ranges from −30 to 30 m/s, and the turbulent wind speed fluctuates randomly around zero with time.

Fig. 14 shows a comparison between the simulated fluctuating wind speed power spectrum and the target power spectrum. The power spectrum of fluctuating wind speed generated by the harmonic synthesis method fits well for low frequencies (10^{-2}~10^{-1} rad), and the simulated curve diverges gradually for high frequencies (10^{0}~10^{1} rad), but still fluctuates near the target curve. Overall, the curve fits well, confirming the accuracy and dependability of our wind field simulation.

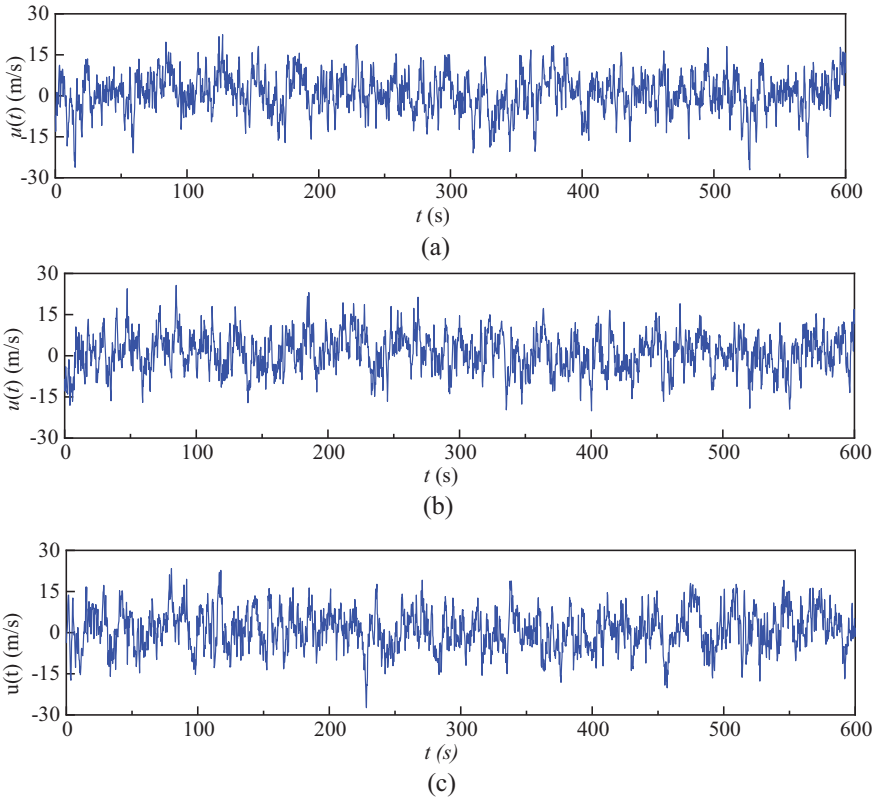

Figure 13: Time history of turbulent wind speed at significant simulation points (a) Measuring point #1; (b) Measuring point #15; (c) Measuring point #24

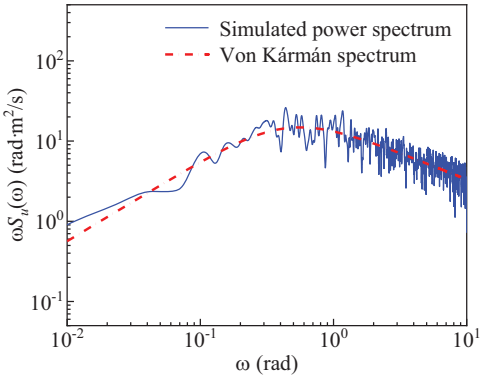

Figure 14: Comparison of the simulated spectrum with the target spectrum (Measuring point #15)

4.2 Buffeting Analysis of the Bridge

4.2.1 Time-Domain Analysis

The random vibration of bridges caused by turbulent wind in atmospheric boundary layers is the main form of bridge buffeting. Common calculation methods for buffeting response mainly include the time-domain buffeting analysis method, and the frequency-domain buffeting analysis method. The frequency-domain buffeting analysis method obtains structural response characteristics by calculating statistical

characteristics of the wind action, which has the advantage of being computationally simple. Since the response of the structure is essentially a transient process, there are limitations in using its statistical characteristics with the frequency domain method [40]. The time-domain method instead converts wind forces into time series and calculates the structural response using FE software. It considers nonlinear effects (which are apparent in long-span flexible bridges) and more accurately represents aerodynamic forces on the bridge. Therefore, we choose the time-domain method to analyze the bridge buffeting response.

To address the unstable characteristics of buffeting forces, Davenport [41] introduced an aerodynamic admittance function (AAF). The formulation of the buffeting force model is derived as outlined below:

$$L_b(t) = \frac{1}{2}\rho U^2 D\left[2C_L\chi_{Lu}\frac{(u(t))}{U} + (C'_L(\alpha)+C_D)\chi_{L\omega}\frac{(\omega(t))}{U}\right] \tag{19}$$

$$D_b(t) = \frac{1}{2}\rho U^2 D\left[2C_D\chi_{Du}\frac{(u(t))}{U} + (C'_D(\alpha)-C_L)\chi_{D\omega}\frac{(\omega(t))}{U}\right] \tag{20}$$

$$M_b(t) = \frac{1}{2}\rho U^2 D^2\left[2C_M\chi_{Mu}\frac{(u(t))}{U} + C'_M(\alpha)\chi_{M\omega}\frac{(\omega(t))}{U}\right] \tag{21}$$

where $L_b(t)$, $D_b(t)$, and $M_b(t)$ represent the lift, drag forces, and pitching moment under the turbulent condition; $C'_L(\alpha)$, $C'_D(\alpha)$, and $C'_M(\alpha)$ denote the derivatives of the coefficients associated with three components of forces (AFC) to angle of attack (α); the definitions of the other parameters are the same as in the previous paragraph. χ_{ab} (the subscript a takes L, D, or M, and b takes u or w) represents the AAF in relation to the horizontal and vertical directions. The Fourier transform can be performed on the above equations, taking into account the power spectra of the fluctuating wind. Subsequently, the expression for the buffeting forces can be represented as follows:

$$S_L(\omega) = (\rho UD)^2\left[C_L{}^2|\chi_{Lu}(\omega)|^2 S_u(\omega) + \frac{1}{4}\left[C'_L(\alpha)+C_D\right]^2|\chi_{L\omega}(\omega)|^2 S_\omega(\omega)\right] \tag{22}$$

$$S_D(\omega) = (\rho UD)^2\left[C_D{}^2|\chi_{Du}(\omega)|^2 S_u(\omega) + \frac{1}{4}\left[C'_D(\alpha)-C_L\right]^2|\chi_{D\omega}(\omega)|^2 S_\omega(\omega)\right] \tag{23}$$

$$S_M(\omega) = (\rho UD^2)^2\left[C_M{}^2|\chi_{Mu}(\omega)|^2 S_u(\omega) + \frac{1}{4}C'_M(\alpha)|\chi_{M\omega}(\omega)|^2 S_\omega(\omega)\right] \tag{24}$$

where ω represents circular frequency; $S_a(\omega)$ (the subscript a takes on L, D, or M) represents the buffeting lift force, buffeting drag force, and buffeting pitching moment; $S_b(\omega)$ (the subscript b takes on u or w) represents the power spectra of the fluctuating wind in the longitudinal and vertical directions; and $|\chi_{ab}(\omega)|^2$ is the aerodynamic admittance function.

4.2.2 Wind Loading Calculation

The buffeting force acting on the bridge is computed using model of buffeting force modified by Davenport, as shown in Eqs. (19)–(21). In these equations, the aerodynamic coefficients are taken from the results in Section 2 when the AoA is 0° and the aerodynamic admittance coefficient is 1. The time series of the simulated buffeting force is shown in Figs. 15–17. As the aspect ratio of the main girder increases, both its width (B) and the three-component force coefficients increase, resulting in a greater buffeting force acting on the suspension bridge's main girder. For main girders characterized by aspect ratios of 12.7, 9.3 and 7.5, the ranges of buffeting drag forces are −16 to 16 m/s, −12 to 12 m/s, and −10 to 10 m/s; the ranges of buffeting lift forces are −12 to 12 m/s, −10 to 10 m/s, and −8 to 8 m/s; and the ranges of buffeting lift moment are −12 to 12 kN·m, −11 to 11 kN·m, and −10 to 10 kN·m, respectively.

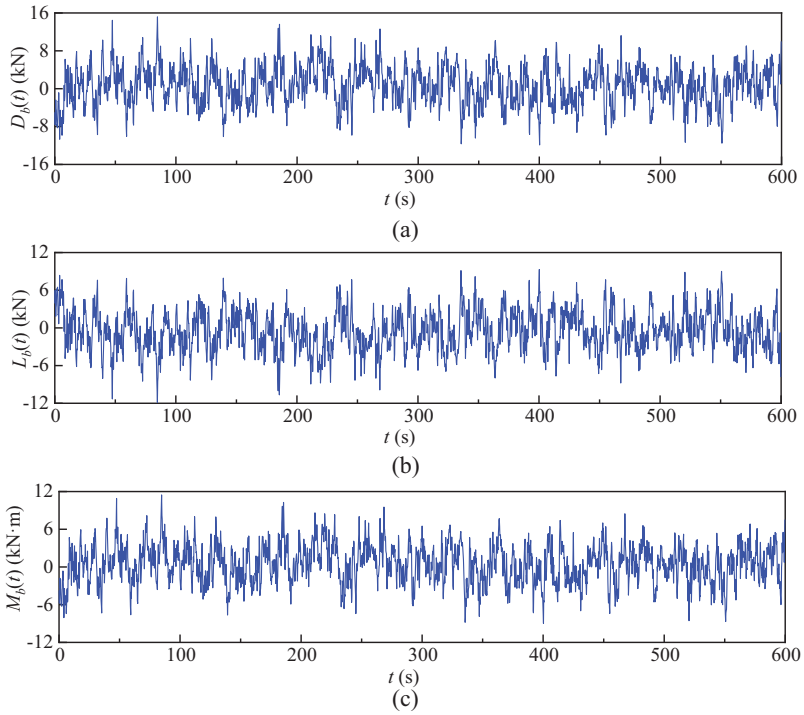

Figure 15: Time history of the buffeting forces at point #15 of Model B-3 (AoA = 0°) (a) Buffeting drag force; (b) Buffeting lift force; (c) Buffeting moment force

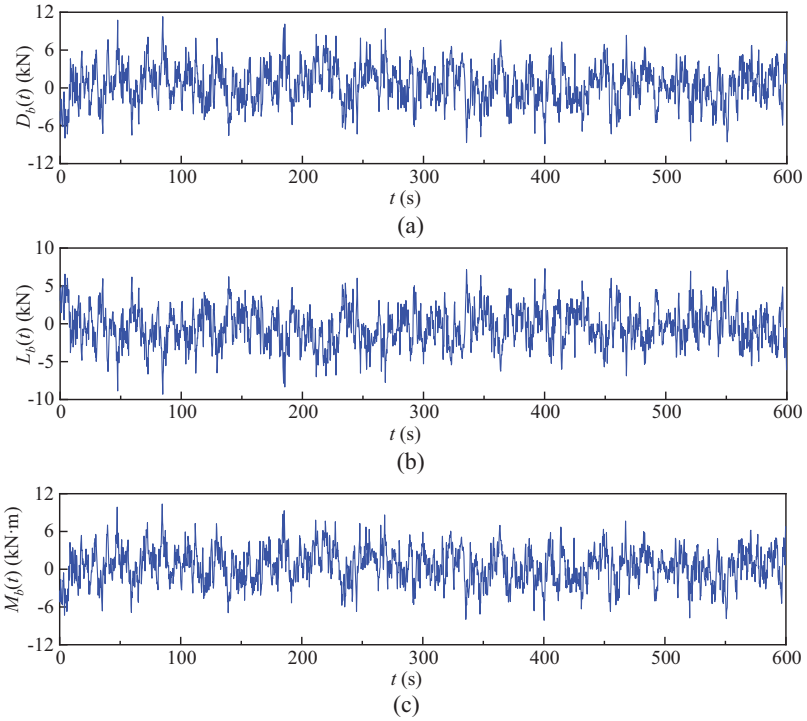

Figure 16: Time history of buffeting forces at point #15 of Model B-2 (AoA = 0°) (a) Buffeting drag force; (b) Buffeting lift force; (c) Buffeting moment force

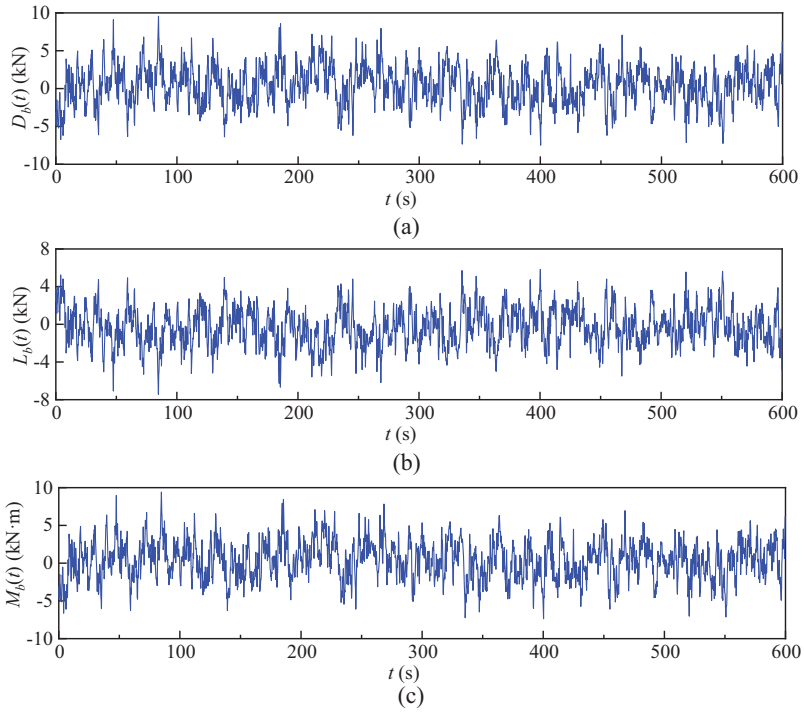

Figure 17: Time history of buffeting forces at point #15 of Model B-1 (AoA = 0°) (a) Buffeting drag force; (b) Buffeting lift force; (c) Buffeting moment force

4.2.3 Buffeting Response Calculation

The analysis of buffeting response in the time domain entails deriving the dynamic equilibrium equation of the bridge for any time t. According to D'Alembert's principle, the formulation for the motion is presented as follows:

$$M\ddot{v}(\mathrm{t}) + \mathrm{C}v(t) + K\dot{v}(t) = P(t) \tag{25}$$

where $P(t)$ indicates the external load of the bridge; M is the mass matrix; C represents the damping matrix; K is the stiffness matrix; $v(t)$, $\dot{v}(t)$ as well as $\ddot{v}(t)$ represent the displacement, velocity, and acceleration vectors. The stiffness matrix expression is:

$$C = \alpha M + \beta K \tag{26}$$

where the mass damping coefficient α and stiffness damping coefficient β are given by:

$$\alpha = \frac{\left(2\omega_i\omega_j\left(\xi_i\omega_j - \xi_j\omega_i\right)\right)}{\left(\omega_j{}^2 - \omega_i{}^2\right)} \tag{27}$$

$$\beta = \frac{\left(2\left(\xi_i\omega_j - \xi_j\omega_i\right)\right)}{\left(\omega_j{}^2 - \omega_i{}^2\right)} \tag{28}$$

Here, ω_i and ω_j represent the ith and jth natural frequencies of the bridge, usually $i = 1$ and $j = 2$; ξ_i and ξ_j represent the damping ratios, taking 0.003 in accordance with the Wind-resistant Specification. Then, we substitute each parameter into the Ansys software for iterative solution.

The analysis of the buffeting response is conducted using Ansys 15.0 [30], utilizing the three-dimensional FE model of the bridge. For a comprehensive description of the model, please refer to

Section 3.2, as detailed information will not be reiterated here to maintain brevity. The time step is 0.125 s and the sampled duration is 600 s. The FE model of a typical suspension bridge (B/D = 12.7) is used and the calculation results are as follows.

Fig. 18 presents the time history of vertical, lateral, and torsional displacement at the midspan over a calculation time of 600 s. The midspan vertical displacement of the main girder is between −0.6 and 0.6 m, the transverse displacement is between −0.6 and 0.9 m, and the torsional displacement is between −0.0015 and 0.0015 rad. The midspan lateral displacement is greater than its vertical displacement, corresponding to first-order symmetric lateral bending during the dynamic characteristic analysis of the bridge. Additionally, the lateral stiffness is significantly less than its vertical stiffness, making lateral displacement more likely to occur than vertical displacement. Due to the large torsional stiffness of the box-type main girder, the torsional displacement values are relatively small.

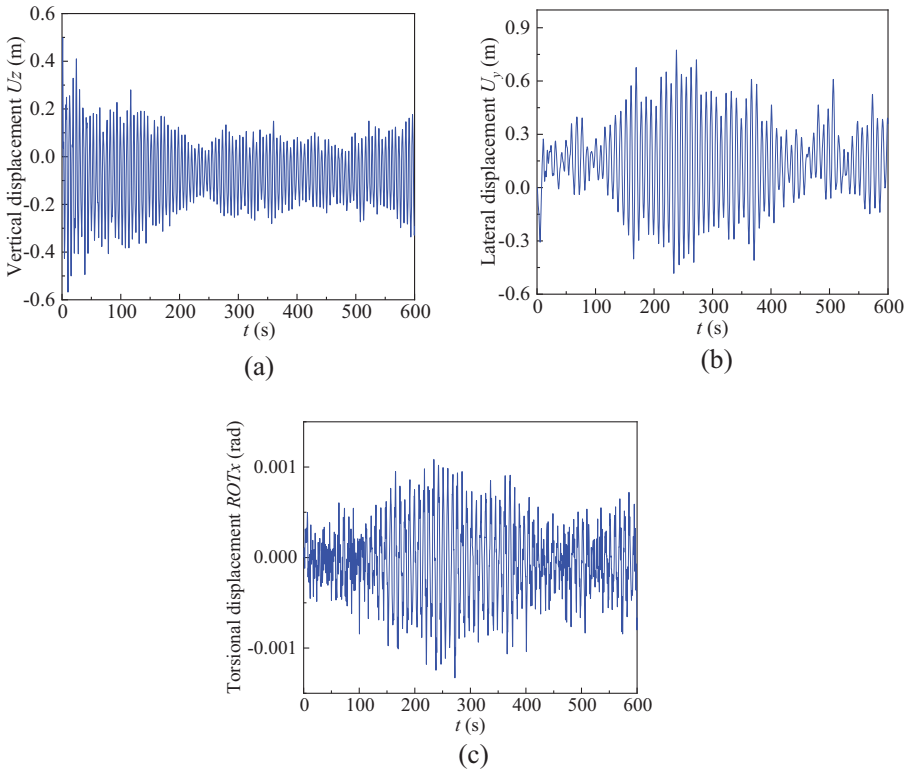

Figure 18: Time history of the buffeting responses at the midspan point on Model B-3 (AoA = 0°) (a) Vertical displacement; (b) Lateral displacement; (c) Torsional displacement

Fig. 19 shows the RMS values of displacement across the entire span of the main girder. The displacement curve of the entire main girder of this bridge type is typically symmetric with respect to the center position. Additionally, the fixed supports at both ends of the bridge restrict the displacement of the main girder, resulting in a trend where the displacements at both ends are smaller and the displacement at the center is larger. Since the second-order mode of the main girder involves antisymmetric vertical bending, while the third and fourth-order modes represent symmetric vertical bending, the superposition of the displacements from these lower-order modes results in three points of maximum vertical displacement along the span of the main girder. Among these, the vertical displacement at the midspan position is the largest. The lateral displacement of

the main girder exhibits a downward-opening parabolic shape, with the maximum lateral displacement occurring at the midspan (1/2 point). The torsional displacement follows a similar pattern to the lateral displacement; however, points of inflection occur at the 1/4 and 3/4 positions along the bridge. This phenomenon is consistent with the variations observed in the vertical displacement.

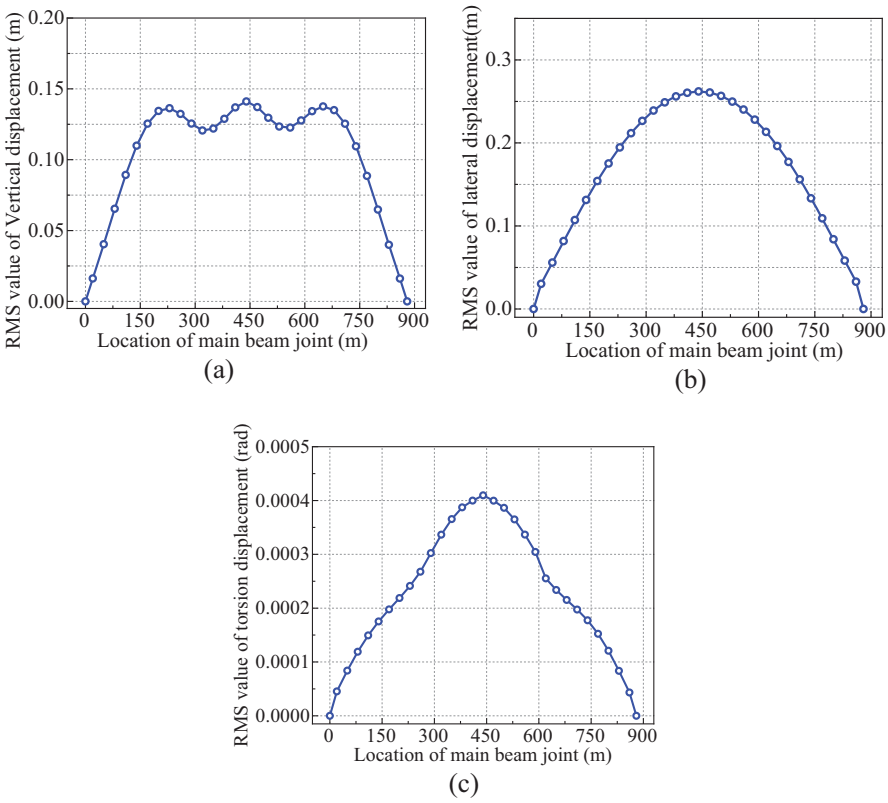

Figure 19: Root mean square (RMS) buffeting displacements of the main girder on Model B-3 (AoA = 0°) (a) Vertical displacement; (b) Lateral displacement; (c) Torsional displacement

4.3 Influence of the Aspect Ratio on the Buffeting Response

In order to examine how varying B/D of main girder on the buffeting force characteristics on the bridge, we referenced the cross-sectional model described in Section 2.1. The height (D) of the main girder is set at 2.7 m, with widths designed as 20.25, 25.11, and 34.2 m, corresponding to aspect ratios of 7.5, 9.3, and 12.7, respectively. These will be referred to as low, medium, and high B/D. Buffeting response analysis of the suspension bridges with different B/D in the same turbulent wind field is conducted, and the results are illustrated in Fig. 20.

Fig. 20 presents the time histories of main girder displacement at the midspan point for different aspect ratios. Within the calculation time of 600 s, the vertical displacement range of the main girder in the midspan is as follows: for the high B/D, the range is −0.568 to 0.498 m; for the medium B/D, the range is −0.667 to 1.278 m; and for the low B/D, the range is −1.321 to 1.93 m. Analysis indicates that a reduction in B/D corresponds to an increase in the vertical displacement amplitude of the main girder. This shows that the deformation of the girder with a small aspect ratio is more significant under the vertical load. The moment of inertia of the girder decreases, resulting in a decrease in its bending resistance, which increases the amplitude. The lateral displacement range of the girder in the midspan is as follows: for the

high B/D, the range is −0.483 to 0.775 m; for the medium B/D, the range is −0.555 to 0.957 m; and for the low B/D, the range is −1.229 to 1.721 m.

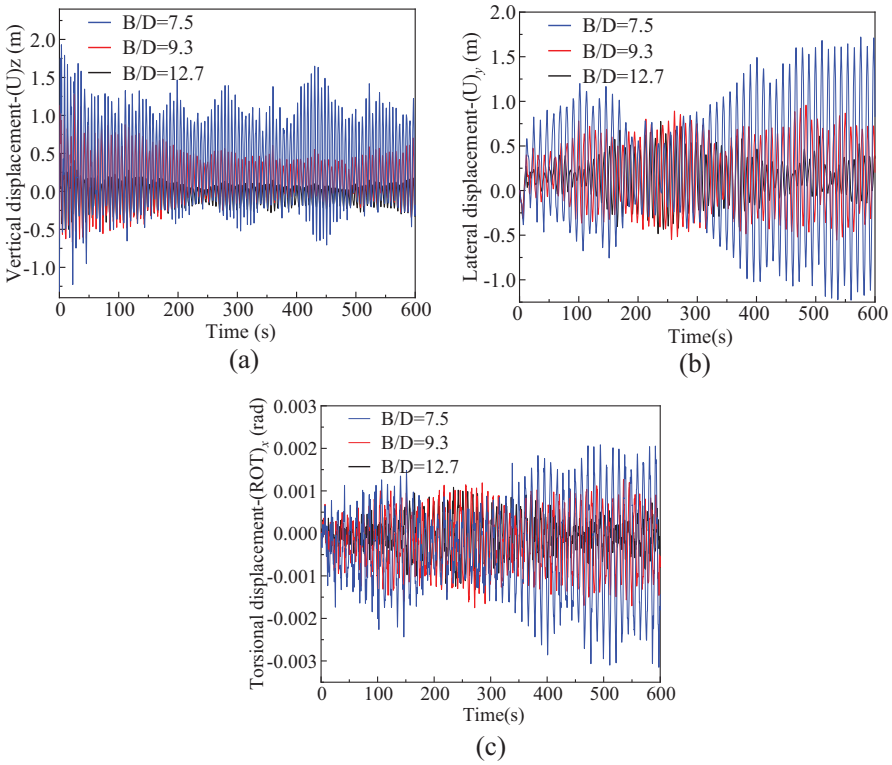

Figure 20: Time history of main girder displacement at the midspan point for varying aspect ratios (AoA = 0°) (a) Vertical displacement; (b) Lateral displacement; (c) Torsional displacement

Similarly, for lateral displacement, a decrease in aspect ratio also results in an elevation of lateral displacement. The smaller B/D makes the deformation of the beam more obvious after the transverse load is absorbed, which is intimately related to the reduction in moment of inertia. Meanwhile, the torsional displacement range of the main girder in the midspan is as follows: for the high B/D, the range is −0.0014 to 0.0011 rad; for the medium B/D, the range is −0.0018 to 0.0013 rad; and for the low B/D, the range is −0.0032 to 0.0021 rad. The reduction in aspect ratio leads to the reductions in the moment of inertia and bending stiffness of the main girder section, so the vibration amplitude of the girder will be larger. Therefore, as the aspect ratio decreases, both the fluctuation range and the mean value of all displacements of the girder progressively increase.

Fig. 21 shows RMS buffeting displacements of the main girder for varying aspect ratios. The data indicate that a decrease in the aspect ratio is associated with a substantial increase in all displacements of the main girder. The disappearance of second-order symmetric vertical bending mode of the main girder (due to the reduced aspect ratio) results in a decrease in the vertical displacements at the 1/4 and 3/4 positions. Therefore, with the reduction of the B/D, the three extreme points of buffeting displacements for the girder gradually disappear. The girder with a smaller aspect ratio has a larger vertical displacement, which indicates that its deformation ability is enhanced under loading. Moreover, the smaller aspect ratio leads to decreases in bending stiffness and stability, which leads to the increase of lateral displacement. Looking at the end position of the main girder, the torsional displacement of the

high aspect ratio girder is greater than that of the medium aspect ratio girder. However, at the 1/4 and 3/4 positions, the torsional displacement of the medium aspect ratio girder rapidly increases and exceeds that of the high aspect ratio case. This phenomenon could be attributed to the torsional stiffness of the girder and its load distribution characteristics. According to the data in this figure, the RMS values of vertical, lateral, and torsional displacements for the medium aspect ratio girder are 3.15, 1.52, and 1.72 times those of the high aspect ratio girder, respectively. Also, the RMS values of vertical, lateral, and torsional displacements for the low aspect ratio girder are 6.35, 2.73, and 2.79 times those of the high aspect ratio girder, respectively.

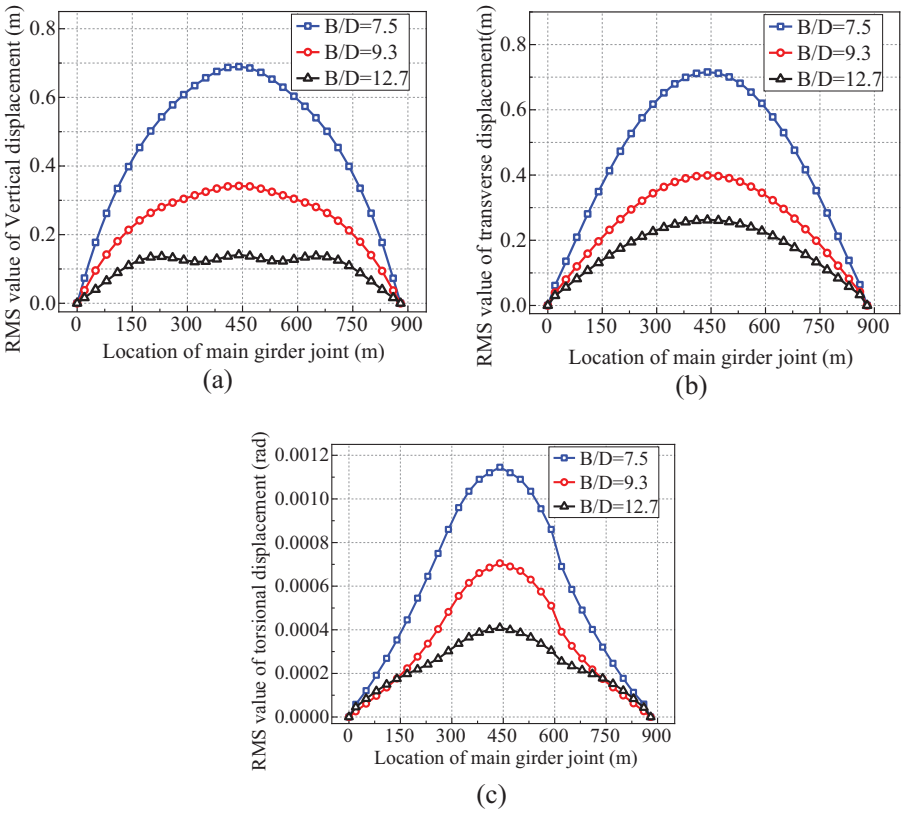

Figure 21: Root mean square (RMS) buffeting displacements of the main girder for varying aspect ratios (AoA = 0°) (a) Vertical displacement; (b) Lateral displacement; (c) Torsional displacement

Fig. 22 shows the reduced RMS buffeting displacements, which are calculated by dividing the RMS buffeting displacements of the three models by the RMS buffeting displacement of Model B-2. Comparing the buffeting displacements in three directions, it becomes evident that the RMS vertical displacement of the main girder is most sensitive to changes in aspect ratio, followed by torsional displacement and then lateral displacement. This is attributed to the fact that vertical aerodynamic force responds more readily to changes in the cross-sectional shape of the beam. Additionally, the reduced RMS value of vertical displacement fluctuates less along the span direction with respect to aspect ratio, showing a relatively stable upward and downward variation. The reduced RMS value of lateral displacement hardly changes along the length of the span. However, the reduced RMS value of torsional displacement fluctuates the most. From the support to the midspan, the torsional displacement becomes increasingly less sensitive to aspect ratio changes.

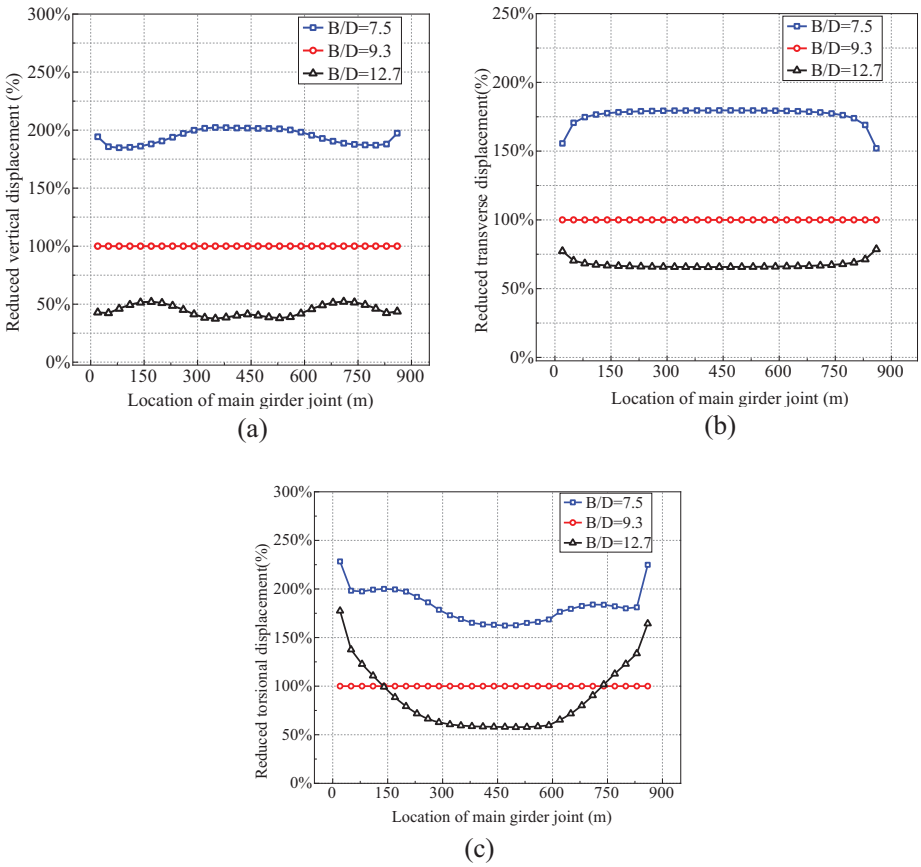

Figure 22: The reduced RMS buffeting displacements of the main girder (the RMS buffeting displacement values of the three models are divided by the buffeting displacement values of Model B-2) (AoA = 0°) (a) Vertical displacement; (b) Lateral displacement; (c) Torsional displacement

From the results above, we can conclude that the B/D of the main girder substantially influences the buffeting response of the bridge. A reduction in the aspect ratio leads to an increase in the range of the displacement, and the RMS values of the displacements also increase significantly. This indicates that a smaller B/D of the main girder, which approaches that of a bluff body, leads to an increased buffeting response of the bridge. Therefore, aspect ratio of the main girder must be considered as a key factor in the design process of a long-span suspension bridge to ensure the structural stability and safety under diverse environmental conditions. This study offers valuable insights for bridge engineers to improve the wind and seismic resistance of bridges, potentially extending their service lives.

5 Conclusions

This study investigated how variations in the aspect ratio (B/D) of the main girder influence buffeting response of long-span suspension bridges. First, numerical models of streamlined box girders with B/D of 7.5, 9.3, and 12.7 were established to study aerodynamic coefficients under different attack angles, using computational fluid dynamics (CFD) simulations. Then, three-dimensional FE models of three long-span suspension bridges with different girders (B/D of 7.5, 9.3, and 12.7) were established in Ansys software, and the dynamic characteristics of these bridges were accordingly obtained. Finally, an inlet turbulent wind field conforming to the target power spectrum was generated using the harmonic synthesis method,

and a time-domain analysis was performed to assess the influence of B/D on the buffeting response characteristics.

It was found that the larger the B/D of the streamlined box girder, the larger the time-averaged and fluctuating drag, lift, and moment coefficients of the main girder. This indicates that a larger aspect ratio causes a larger windward area of the beam, resulting in greater aerodynamic forces. At small angles of attack ($0° \leq \alpha \leq 4°$), the time-averaged drag coefficient is insensitive to the aspect ratio. With the increase of AoA, the influence of aspect ratio on the time-averaged drag, lift, and moment coefficients of the main girder becomes greater. This may be because the larger AoA makes flow separation and pressure distribution changes more pronounced.

In the turbulent wind field, the RMS value of buffeting displacement of the main girder was at a minimum at both ends, and increased gradually towards the midspan, due to the distribution of wind loads over the entire length of the bridge. It is noteworthy that when B/D is 12.7, the RMS value of vertical displacement has three extreme points along the spanwise direction, representing the contribution of the first order antisymmetric vertical bending mode.

With the reduction of B/D, the smaller the stiffness of the bridge structure, the smaller the structural damping, and the smaller the natural vibration frequency of the bridge. Furthermore, a decrease in B/D causes a reduction in the moment of inertia of the main girder, which in turn increases the amplitude of vibrations; the dynamic characteristics of the bridge can cause even greater displacement. Consequently, the range of the displacement will increase, and the RMS buffeting displacements will also increase. Therefore, different main girder aspect ratios markedly influence the buffeting response; notably, a smaller aspect ratio corresponds to a greater buffeting response.

By comparing the buffeting displacements of the main girder in three directions, we found that the RMS value of vertical displacement is most sensitive to the change of aspect ratio, followed by changes in torsional displacement and lateral displacement. This phenomenon occurs because the vertical aerodynamic force responds more acutely to changes in the beam's cross-sectional shape.

Generally, this research primarily investigated how the B/D of the main girder affects the buffeting response. By understanding the effect of aspect ratio on buffeting, engineers can optimize the geometric design of bridges to reduce buffeting-induced fatigue damage, thereby improving structural safety under extreme wind conditions. This optimization can be actualized by adjusting existing bridge design schemes, for example changing the aspect ratio of the girder to reduce the effect of turbulence on the buffeting. It is important to highlight that the results of this research are derived from streamlined box girders and long-span suspension bridges. Future research can expand the scope to investigate other main girder sections and different types of bridges. Extending the research to these structures will provide a comprehensive evaluation of their buffeting responses under wind loads, and enhance the overall understanding of bridge wind resistance.

Acknowledgement: The authors express their sincere gratitude to Bo Wu for the invaluable guidance and constructive suggestions offered throughout the preparation of this manuscript; his expertise significantly contributed to the advancement of this research.

Funding Statement: This work is funded by the National Natural Science Foundation of China (Grant No. 52108435), the Science and Technology Research Program of Chongqing Municipal Education Commission (Grant No. KJQN202404320), Chongqing Jiaotong University Postgraduate Research and Innovation Project (2024S0013), and Chongqing Jiaotong University Undergraduate Innovation and Entrepreneurship Project (S202410618019).

Author Contributions: Jingxiang Zhou: Writing—original draft preparation; formal analysis; methodology; Qiaoling Zhou: Conceptualization; formal analysis; investigation; methodology; writing—original draft preparation; writing—review and editing; project administration. Chunlian Liang and Yulu Guo: Formal analysis; investigation; writing—original draft preparation; visualization; Zhao Xiao: Resources, data curation; Yingfeng Xu: Investigation. All authors reviewed the results and approved the final version of the manuscript.

Availability of Data and Materials: The data that support the findings of this study are available from the corresponding author upon reasonable request.

Ethics Approval: Not applicable.

Conflicts of Interest: The authors declare no conflicts of interest to report regarding the present study.

References

1. Toyota Y, Hirose T, Ono S, Shidara K. Experimental study on vibration characteristics of prestressed concrete beam. Procedia Eng. 2017;171:1165–72. doi:10.1016/j.proeng.2017.01.483.
2. Bonopera M, Liao WC, Perceka W. Experimental-theoretical investigation of the short-term vibration response of uncracked prestressed concrete members under long-age conditions. Structures. 2021;35(3):260–73. doi:10.1016/j.istruc.2021.10.093.
3. Wu B, Zhou JT, Li SP, Xin JZ, Zhang H, Yang XY. Combining active and passive wind tunnel tests to determine the aerodynamic admittances of a bridge girder. J Wind Eng Ind Aerodyn. 2022;231(1):105180. doi:10.1016/j.jweia.2022.105180.
4. He XH, Li H, Wang HF, Fang DX, Liu MT. Effects of geometrical parameters on the aerodynamic characteristics of a streamlined flat box girder. J Wind Eng Ind Aerodyn. 2017;170(1):56–67. doi:10.1016/j.jweia.2017.08.009.
5. Ma TT, Zhao L, Cao SY, Ge YJ, Miyagi H. Investigations of aerodynamic effects on streamlined box girder using two-dimensional actively-controlled oncoming flow. J Wind Eng Ind Aerodyn. 2013;122:118–329. doi:10.1016/j.jweia.2013.07.011.
6. Li HH, Zhang LL, Wu B, Ni ZJ, Yang Y. Effects of the angle of attack on the aerodyna-mic characteristics of a streamlined box girder. Adv Struct. 2021;24(10):2090–104. doi:10.1177/1369433221992490.
7. Li M, Li MS, Sun YG. Effects of turbulence integral scale on the buffeting response of a long-span suspension bridge. J Sound Vib. 2020;490(1–2):115721. doi:10.1016/j.jsv.2020.115721.
8. Zhou YF, Zhao L, Ge YJ. Analysis of the effect of turbulence integral scale on bridge jitter response. Shock Vib. 2010;29(8):87–93.
9. Mao JX, Wang H, Tao TY, Xu ZD, Li AQ. Effect of turbulent spatial correlation coefficient on the buffeting response of long-span three-tower suspension bridge. J Sound Vib. 2016;35(10):202–6.
10. Vaz DC, Almeida RAB, Didier E, Urgueira APV, Borges ARJ. Improving the aerodynamic performance of Vila-Real Bridge deck-section. J Wind Eng Ind Aerodyn. 2016;156:72–83. doi:10.1016/j.jweia.2016.07.002.
11. Larsen A, Wall A. Shaping of bridge box girders to avoid vortex shedding response. J Wind Eng Ind Aerodyn. 2012;104–106(14):159–65. doi:10.1016/j.jweia.2012.04.018.
12. Nagao F, Utsunomiya H, Oryu T, Manabe S. Aerodynamic efficiency of triangular fairing on box girder bridge. J Wind Eng Ind Aerodyn. 1993;49(1–3):565–74. doi:10.1016/0167-6105(93)90050-X.
13. Sukamta NF, Noda M, Muneta K. Aerodynamic stabilizing mechanism of a cable stayed bridge with two edge box girder. In: Proceedings of 6th International Colloquium on Bluff Body Aerodynamics and Applications, 2008; Milano, Italy.
14. Haque M, Katsuchi H, Yamada H, Nishio M. Investigation of edge fairing shaping effects on aerodynamic response of long-span bridge deck by unsteady RANS. Arch Civ Mech Eng. 2016;16(4):888–900. doi:10.1016/j.acme.2016.06.007.

15. Kusano I, Montoya CM, Baldomir A, Nieto F, Jurado JÁ, Hernández S. Reliability based design optimization for bridge girder shape and plate thicknesses of long-span suspension bridges considering aeroelastic constraint. J Wind Eng Ind Aerodyn. 2020;202(9):104176. doi:10.1016/j.jweia.2020.104176.
16. Zheng J, Fang GS, Wang ZL, Zhao L, Ge YJ. Shape optimization of closed-box girder considering dynamic and aerodynamic effects on flutter: a CFD-enabled and Kriging surrogate-based strategy. Eng Appl Comp Fluid. 2023;17(1):2191693. doi:10.1080/19942060.2023.2191693.
17. Tinmitondé S, He XH, Lei Y. Single-objective aerodynamic optimization of a streamlined bridge deck subjected to shape modification using a polynomial emulator and genetic algorithm. Struct *Multidisc Optim*. 2022;65(12):356.
18. Bernardini E, Spence MS, Wei D, Kareem A. Aerodynamic shape optimization of civil structures: a CFD-enabled Kriging-based approach. J Wind Eng Ind Aerodyn. 2015;144:154–64.
19. Montoya CM, Hernández S, Nieto F. Shape optimization of streamlined decks of cable-stayed bridges considering aeroelastic and structural constraints. J Wind Eng Ind Aerodyn. 2018;177:429–55.
20. Montoya CM, Nieto F, Hernández S, Kusano I, Álvarez AJ, Jurado JÁ. CFD-based aeroelastic characterization of streamlined bridge deck cross-sections subject to shape modifications using surrogate models. J Wind Eng Ind Aerodyn. 2018;177:405–28.
21. Parker R, Welsh MC. Effects of sound on flow separation from blunt flat plates. Int J Heat Fluid Fl. 1983;4(2): 113–27.
22. Shimada K, Ishihara T. Application of a modified k–ε model to the prediction of aerodynamic characteristics of rectangular cross-section cylinders. J Fluid Struct. 2002;16(4):465–85.
23. Beitel A, Heng H, Sumner D. The effect of aspect ratio on the aerodynamic forces and bending moment for a surface-mounted finite-height cylinder. J Wind Eng Ind Aerodyn. 2019;186:204–13.
24. Ma W, Huang BC, Zheng DQ, Lu M, Li HY. Effect of the presence of end plates and aspect ratio on the aerodynamic forces on circular cylinders in various flow regimes. Fluid Dyn Res. 2019;51(5):055503.
25. Xing JT, Masoud R, Dai HL, Wei-Hsin L. Investigating the coupled effect of different aspect ratios and leeward protrusion lengths on vortex-induced vibration (VIV)-galloping energy harvesting: modelling and experimental validation. J Sound Vib. 2024;568:118054.
26. Yang J, He XH, Ran RF, Jiang C. Numerical simulation analysis of the three-component force coefficient of continuous beam bridge in high-speed railway. J Railway Sci Eng. 2013;1:11–5.
27. Zhang LL. Numerical simulation of vortex-induced vibration of typical bridge sections based on Overset Mesh (Master's Dissertation). Changan University: Xi'an, China; 2018.
28. Yang YX, Zhu JB, Hong LZ, Ge YJ, Su RS, Yang HC, et al. Effect mechanism of wind barriers on flutter characteristics of closed box girders with different aspect ratios. J Bridge Eng. 2023;28(9):152. doi:10.1061/JBENF2.BEENG-6079.
29. Xue ZS, Zhou JC, Xiao Z, Deng X. Investigation of the aerodynamic characteristics of single-box girders with different aspect ratios. Vibroeng Procedia. 2023;53:78–83. doi:10.21595/vp.
30. Ansys Inc. ANSYS Release 15.0. Ansys Inc; 2013. Available from: https://www.ansys.com. [Accessed 2024].
31. Wu B, Li SP, Li K, Zhang LL. Numerical and experimental studies on the aerodynamics of a 5:1 rectangular cylinder at angles of attack. J Wind Eng Ind Aerodyn. 2020;199(3):104097. doi:10.1016/j.jweia.2020.104097.
32. Baetke F, Werner H, Wengle H. Numerical simulation of turbulent flow over surface-mountedobstacles with sharp edges and cornersIl. J Wind Eng Ind Aerodyn. 1990;35(231):129–47. doi:10.1016/0167-6105(90)90213-V.
33. Yang Y, Li L, Yao G, Wang M, Zhou CW, Lei T, et al. Study on the influence of the fully enclosed barrier on the vortex-induced vibration performance of a long-span highway-railway double-deck truss bridge. Phys Fluids. 2024;36(8):087132. doi:10.1063/5.0220758.
34. Yao G, Yang Y, Wu B, Liu LJ, Zhang LL. Aerodynamic admittance influence on buffeting performance of suspension bridge with streamlined deck. J Vibroeng. 2019;21(1):198–214.
35. Wang H, Xu ZD, Yang M, Tao TY, Mao JX, Gao H. Numerical analysis on buffeting performance of a long-span four-tower suspension bridge using the FEM model. KSCE J Civ Eng. 2021;25(3):1–12. doi:10.1007/s12205-021-2406-6.

36. Liu ZH, Fang GS, Zhao L, Ge YJ. Uncertainty propagation of turbulence parameters for typhoon and Non-typhoon winds in buffeting analysis of Long-span bridges. Eng Struct. 2023;291:116491. doi:10.1016/j.engstruct.2023.116491.
37. Zhao L, Wang ZL, Chen WL, Cui W. Buffeting performance of long-span bridges with different span affected by parametric typhoon wind. J Wind Eng Ind Aerodyn. 2024;254(12):105903. doi:10.1016/j.jweia.2024.105903.
38. Guo SL, Zhong TY, Yan ZG. Calculation method of buffeting response of cables of long-span cable-stayed bridges. J Jilin Univ (Eng Technol Ed). 2021;51(5):1756–62 (In Chinese).
39. Rice SO. Mathematical analysis of random noise. Bell Syst Techn J. 1944;23(3):282–332. doi:10.1002/j.1538-7305.1944.tb00874.x.
40. Chen ZQ. Wind engineering of bridge. Beijing: China Communications Press; 2005.
41. Davenport AG. Buffetting of a suspension bridge by storm winds. J Struct. 1962;88(3):233–70. doi:10.1061/JSDEAG.0000773.